NORTHWESTERN UNIVERSITY

Quantifying Hemodynamic Compromise and Stroke Risk Using Magnetic Resonance Imaging

A DISSERTATION

SUBMITTED TO THE GRADUATE SCHOOL
IN PARTIAL FULFILLMENT OF THE REQUIREMENTS

for the degree

DOCTOR OF PHILOSOPHY

Field of Biomedical Engineering

By

Charles Cantrell

EVANSTON, ILLINOIS

December 2016

Abstract

Stroke is the leading cause of death and long term disability in the industrialized world. With the current population aging, the number of individuals at risk of stroke along with the associated health care costs are anticipated to rise considerably in the coming years. Consequently, there is an unmet need to identify high risk patients so that prophylactic medical management may prevent this devastating event. In this thesis, we discuss several magnetic resonance imaging (MRI) protocols that model underlying cerebral hemodynamic processes involved in stroke. Specifically, with regards to ischemic stroke, we present a novel imaging method to measure oxygen extraction fraction and show that it correlates with hemodynamic compromise in patients with intracranial atherosclerotic disease. Furthermore, we validate an MR technique for quantifying cerebrovascular reserve (CVR) in an animal model, and show it correlates with the stage of hemodynamic compromise. Lastly, we examine hemorrhagic stroke and propose a new imaging metric associated with aneurysm rupture risk and wall thickness.

Table of Contents

List of Figures

List of Tables

Chapter 1 Introduction

1.1 Significance

The overarching and long term goal of this volume of work is to improve the diagnosis and treatment of patients at risk of stroke. There are two main types of stroke, ischemic and hemorrhagic, both of which are studied in this thesis. Ischemic stroke is the result of a blood clot that blocks a blood vessel feeding a specific portion of the brain, consequently, reducing the amount of oxygen available. Hemorrhagic stroke, on the other hand, is caused by ruptured blood vessels that result in brain bleeding. Regardless of type, stroke is a devastating event. In this work we present three magnetic resonance imaging (MRI) techniques that can be used to quantify patient stroke risk.

Ischemic stroke is the leading cause of death and disability in the industrialized world (1) and accounts for approximately 87% of all strokes (2). With the population aging, the number of individuals at risk for stroke along with the associated health care cost is anticipated to rise considerably in the coming years. Consequently, there is an unmet need to identify patients who are most likely to suffer an ischemic stroke so that steps can be taken to prevent this devastating event. Significant work has already gone into quantifying stroke risk with advanced imaging; however, unfortunately, there exists no widely available means for doing so. Through positron emission tomography (PET), however, Dr. Colin Derdeyn and colleagues have shown that oxygen extraction fraction (OEF) is an independent indicator of stroke (3), with 12% hemispheric asymmetry indicating significant risk for a future stroke (4). OEF-PET images, however, require an on-site cyclotron due to the short half-life (~11 min.) of the tracer which has

hindered its growth outside academic environments. Currently, fewer than 10 PET sites exist within the United States that can image OEF.

Hemorrhagic stroke accounts for the remaining 13% of stroke cases. Though fewer in number than ischemic stroke, risk of hemorrhage affects a substantial portion of the population. Some studies suggest that upwards of 6% of the general population harbors an intracranial aneurysm (IA) (5). While the vast majority of IAs remain dormant, approximately 30,000 rupture annually in the U.S. alone (5) causing devastating intracranial subarachnoid hemorrhage complications. Because of the inherent treatment risks associated with microsurgical clipping or endovascular coil embolization and the fact that only a small fraction of IAs rupture annually (<2%), treatment of unruptured IAs remains controversial (6,7). Considering, IAs account for nearly 85% of all hemorrhagic strokes (8), a methodology to differentiate high rupture risk is greatly needed in the clinical environment.

1.2 Objectives

The long-term goal of this research is to create and improve the diagnostic tools available for patients at risk of stroke. We have done this by developing the following new MR acquisition, reconstruction, and post-reconstruction imaging techniques needed to quantify patient risk.

1. We developed a novel MR-OEF imaging method in three steps:
    a. We designed and implemented a cardiac gated rosette trajectory to measure intracranial transient susceptibility fluctuations. We show these susceptibility fluctuations are a consequence of altering ratios of oxygenated vs deoxygenated

hemoglobin throughout the cardiac cycle and correlate them with cerebral hemodynamic failure in patients with intracranial atherosclerotic disease. Finally, we propose a vascular residue function based on the Windkessel model, which correlates with CVR.

b. We created a new iterative progressive length conjugate gradient, non-linear least squares reconstruction algorithm to improve image quality.

c. We created and implemented a new post-processing technique for removing static field inhomogeneity. We show that using independent component analysis (ICA) to remove background field artifact, improves correlation with hemodynamic compromise.

2. We implemented and verified a method for quantifying cerebral vascular reserve in three steps:

   a. We validated the accuracy of the Bookend technique in quantifying CBF in back to back injections of contrast agent by implementing a second injection specific water correction factor.

   b. We validated the technique in an animal model, and show high correlation in qCBF and qCVR with microspheres.

   c. We performed a retrospective study on a series of consecutive patients with angiographically confirmed cerebral vascular disease who underwent an ACZ challenge MRI perfusion study as part of their standard of care. We show qCVR correlates with hemodynamic compromise.

3. We created a new parameter for measuring contrast leakage through an aneurysm wall, and show its association with rupture risk. Furthermore, we developed a rapid method to determine diffusional effects using parameterization based on easily accessible ADC values, which may preclude the need for iterative diffusion-compensated fitting.

1.3 Organization

Following a discussion of pertinent underlying principles of MRI physics in Chapter 2, Chapter 3 will discuss cerebral autoregulation, while Chapters 4-6 will discuss the author's contribution to stroke risk imaging. An overview at the beginning of each chapter has been added to describe any relevant background information, the purpose for each study, and the author's contribution to the volume of work. Chapter 4 will examine MR-OEF, where we will discuss the rosette trajectory, the iterative PLCG reconstruction method, and the use of ICA for filtering background susceptibility artifact. Chapter 5 will explore quantitative CVR, where our second injection correction will be presented. Chapter 6 will explore the avenue of hemorrhagic stroke (aneurysm rupture), where we will discuss contrast leakage through the aneurysm wall and a parameterization method to reduce required computational time. Finally, Chapter 7 will discuss conclusions and areas for future work.

Chapter 2 Magnetic Resonance Fundamentals

2.1 Spin Physics

Unlike photography or x-ray imaging where photons directly interact with the imaging medium, MR occurs in a roundabout manner. In MRI, the signal is acquired from the precession of a bulk magnetic moment which is, in turn, converted into an image. This magnetic moment is a result of a fundamental atomic property called spin. In effect, atoms with an odd atomic weight spin around their axis in the presence of an external magnetic field, generating a magnetic dipole moment following Equation 1,

$$\vec{\mu} = \gamma \vec{s} \tag{1}$$

where, $\vec{\mu}$ is the magnetic dipole moment, γ is the gyromagnetic ratio of the atom, and $\vec{s}$ is the angular momentum (spin) of the atom. Table 1 shows gyromagnetic ratios and relative sensitivities (dependent on γ and abundance) of nuclei with non-zero magnetic moments abundant in the body.

Table 1 Gyromagnetic ratios and relative sensitivities of abundant human nuclei

Nucleus	Symbol	Gyromagnetic Ratio (MHz/T)	Relative Sensitivity
Hydrogen – 1	^{1}H	42.575	1.000
Carbon - 13	^{13}C	10.705	0.016
Fluorine - 19	^{19}F	40.054	0.083
Sodium – 23	^{23}Na	11.262	0.093
Phosphorus -31	^{31}P	17.235	0.066

As can be seen in Table 1, in vivo imaging is most sensitive to hydrogen atoms, ^{1}H, a result of the vast amounts of water present in tissue. Consequently, in vivo MRI most commonly

images hydrogen, though in certain circumstances can be done with the other nuclei shown in Table 1.

Bulk magnetization is the net vector effect of all the individual ^{1}H protons in the body (order of 10^{23}). In the absence of an external magnetic field, the magnetic moments of the ^{1}H protons will be randomly oriented, resulting in a bulk magnetization of M = 0. However, in the presence of an external field, B_0, the ^{1}H protons orient themselves in a meaningful manner. Because, atoms have quantum properties, a proton's orientation will be discrete—either parallel or anti-parallel to the external field. The ratio of the number of parallel $N_\uparrow$ and anti-parallel $N_\downarrow$ hydrogen atoms is related to energy difference between states, ΔE, and the temperature of the system, T, given by Boltzmann's Equation 2

$$\frac{\boldsymbol{N_\uparrow}}{\boldsymbol{N_\downarrow}} = \boldsymbol{e^{\frac{\Delta E}{KT}}} \tag{2}$$

where K is Boltzmann's constant. The ratio of $N_\uparrow$ to $N_\downarrow$ hydrogen atoms provides a bulk magnetization M > 0. In a laboratory environment, where T=300K, B_0 = 1.5 T, there would be about 5 excess parallel spins per 1 million ^{1}H protons or in 1 mL of water approximately 0.3 x 10^{15} excess spins – a small but measurable amount.

Similar to a spinning top precessing about its axis due to gravity, M has its own angular momentum. Consequently, it will not simply align with B_0, but rather it will precess about B_0. This precession has angular frequency, ω_0, described as the Larmor frequency, Equation 3,

$$\boldsymbol{\omega_0 = \gamma B_0} \tag{3}$$

2.2 The Rotating Frame, Excitation and the Bloch Equations

In order to facilitate the discussion of spin excitation, relaxation, and signal acquisition it is customary to work within the rotating frame of reference. The rotating-frame rotates around B_0 with the Larmor frequency, ω_0. Consequently, rotational frequencies occur relative to the on-resonance frequency, ω_0. For the remainder of this thesis, we will work within the rotating frame unless explicitly stated otherwise.

Excitation

At rest, the bulk magnetization lies fully along the main magnetic field (z-axis), or $M_0 = M_z$. In order to measure the bulk magnetization, it must first be tipped away from the z-axis in a process called excitation. Essentially, excitation converts, longitudinal M_z into measurable transverse M_{xy}. Excitation is performed by playing a spinning radiofrequency (RF) pulse, B_1. The B_1 pulse is typically played at the Larmor frequency to excite only on-resonance species precessing with the same frequency. The amount of transverse magnetization can be varied by the flip angle, α, which is a function of the the duration of the B_1 field, τ.

$$\boldsymbol{\alpha = \int_0^{\tau} \gamma B_1(t)\, dt} \tag{4}$$

The flip angle describes the amount of the net magnetization that is flipped into the transverse plane. For simplicity we estimate the RF pulse as instantaneous (occurring at t = 0). Let $t = 0_-$, denote the time immediately before the RF-pulse, and $t = 0_+$ the time immediately following the RF-pulse. Then the longitudinal and transverse can be written as in Equations 5 and 6 respectively.

$$\boldsymbol{M_z(0_+) = M_z(0_-)\cos\alpha - M_{xy}(0_-)\sin\alpha} \quad (5)$$

$$\boldsymbol{M_{xy}(0_+) = M_z(0_+)\sin\alpha + M_{xy}(0_-)\cos\alpha} \quad (6)$$

The transverse magnetization precesses (in the laboratory frame), across laboratory stationary receiver coils creating magnetic flux, which in turn induces a measurable electric current—creating the basis of MR imaging.

Relaxation and the Bloch Equations

Immediately following excitation the system will begin to relax toward equilibrium. The rate of this relaxation is determined by two tissue specific constants (T_1, and T_2). T_1 relates to the longitudinal regrowth and is governed by the loss of excitation energy as a result of energy exchange between nuclei and the surrounding lattice, often referred to as "spin-lattice" relaxation. T_2 relates to transverse relaxation and is a result of dephasing, or the loss of coherence of the net magnetization, referred to as "spin-spin" relaxation. It is important to note, that any process causing T_1 relaxation also causes T_2 relaxation—consequently, T_2 will always be small than T_1 ($T_2 < T_1$). The relaxation process of the net magnetization is described by the Bloch Equation (Equation 7), where **M** is the net magnetization vector, **B** is the applied magnetic field (combination of B_0, B_1 and gradient fields), M_x, M_y, and M_z are the portions of the net magnetizations in the x, y and z directions respectively.

$$\frac{\boldsymbol{dM}}{\boldsymbol{dt}} = \boldsymbol{M \times \gamma B} - \frac{\boldsymbol{M_x i + M_y j}}{\boldsymbol{T_2}} - \frac{\boldsymbol{M_z - M_0}}{\boldsymbol{T_1}}\boldsymbol{k} \quad (7)$$

To examine how T_1 and T_2 affect net magnetization, we solve the Bloch Equation. Working in the rotating frame and assuming the bulk is exposed to a constant external field such that $\Delta B_0(t) = 0$, and there is no applied B_1, we see that the Bloch equation (along the z-axis) simplifies to Equation (8).

$$\frac{\boldsymbol{dM_z(t)}}{\boldsymbol{dt}} = \frac{\boldsymbol{M_z(t) - M_0}}{\boldsymbol{T_1}} \tag{8}$$

The above differential can be solved to show that the regrowth of M_z occurs at an exponential rate described by Equation 9.

$$\boldsymbol{M_z(t) = M_0 + [M_z(0_+) - M_0]e^{-\frac{t}{T_1}}} \tag{9}$$

Making the same assumptions as above we can show the net magnetization in the transverse plane follows the differential in Equation 10.

$$\frac{\boldsymbol{dM_{xy}}}{\boldsymbol{dt}} = -\frac{\boldsymbol{M_{xy}}}{\boldsymbol{T_2}} \tag{10}$$

Equation 10 can be easily solved to show, the transverse magnetization, M_{xy}, decays exponentially (Equation 11).

$$\boldsymbol{M_{xy}(t) = M_{xy}(0_+)e^{-\frac{t}{T_2}}} \tag{11}$$

T_1 and T_2 play an important role in MR imaging because they are tissue dependent (i.e. different tissues have different T_1 and T_2 values).

In practice, another important relaxation rate comes into play, T_2'. T_2' is caused by field inhomogeneities which cause spin phase incoherence. This incoherence results in exponential net magnetization loss in the transverse plane—killing signal. Both transverse decay terms are often grouped into an overall transverse relaxation rate T_2*, defined by

$$\frac{\boldsymbol{1}}{\boldsymbol{T_2^*}} = \frac{\boldsymbol{1}}{\boldsymbol{T_2'}} + \frac{\boldsymbol{1}}{\boldsymbol{T_2}} \tag{12}$$

2.3 Image Formation

Measuring bulk magnetization alone does not create an image, instead we must also employ the use of spatial encoding. Spatial encoding is achieved by applying magnetic gradients (much smaller than the B_0 field). The applied gradients vary spatially along x, y and z. Furthermore, by varying these gradients with time, we can traverse the frequency domain, referred to as k-space. When enough frequency information is collected, an image is created by applying a Fourier Transform. Each of these steps is discussed in more detail below.

2D Slice Selection

One method to impart spatial encoding along the z-direction is to apply a 2D slice selection RF excitation pulse. A 2D slice selection pulse is done by applying a z-gradient, such that $\mathbf{B}=B_0+G\cdot\mathbf{z}$, where G is the strength of the applied gradient. Because the RF-pulse excites only spins precessing at the same frequency of the RF, the application of a z-gradient allows for excitation of spins only in a particular volume along z. Furthermore, the thickness of this slice can be set by altering the gradient strength, G.

Phase and Frequency Encoding

Once spatial information is encoded along the z direction, via 2D slice selection, we must somehow encode along the x and y directions. This is done by phase and frequency encoding. Phase encoding is typically done along the y direction by temporarily applying a y-gradient called the phase encoding gradient. During the duration of the gradient, the spins will precess at different rates based on y-location. After a short duration the gradient is turned off and the spins return to the same Larmor frequency, however, phase has been accrued based on location along the y-axis. To spatially encode along the x axis a readout gradient is employed. The readout

gradient is applied during signal sampling (thus the name "readout"). In this case, the x gradient causes spins to have different frequencies based on location along the x-axis. When fully combined (the spatial encoding along the x, y, and z directions), this acquires one line of *k*-space. The process is repeated with a different phase encoding gradient to acquire a slightly different line, and the process is repeated until all of *k*-space is acquired. Once all of k-space is acquired, a new slice selecting pulse is done, and the process is repeated for each slice of interest. When completed, the Fourier transform is used to convert the acquired *k*-space into the image domain.

The process described above (phase and frequency encoding), is typically described as traversing *k*-space. The phase encoding process of applying a y-gradient moves us along k_y, while the frequency encoding moves us along k_x. The required sampling density to prevent wrapping artifact, where image information is improperly placed, is governed by the Nyquist sampling criteria Equations 13 and 14.

$$\Delta \boldsymbol{t} \leq \frac{\boldsymbol{2\pi}}{\boldsymbol{\gamma |G_x| FOV_x}} \tag{13}$$

$$\Delta \boldsymbol{G_y} \leq \frac{\boldsymbol{2\pi}}{\boldsymbol{\gamma T_{PE} FOV_y}} \tag{14}$$

We see that the, readout sampling interval Δt, is governed by the frequency encoding gradient amplitude, G_x, and the field of view, FOV_x. Similarly, the phase encoding gradient step is a function of the phase encoding time interval, T_{PE} and the field of view, FOV_y.

Cartesian Sampling

One of the most common techniques to acquire k-space is with simple Cartesian sampling. Figure **2.1** is a schematic showing, on the left, how the gradients traverse through k-space, and on the right is a pulse sequence diagram. In Cartesian sampling, a small number of

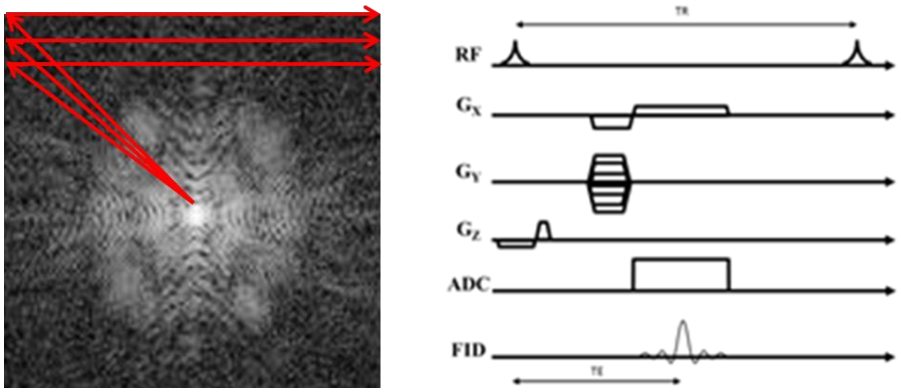

Figure 2.1: Schematic of Cartesian trajectory. (a) traversing k-space (b) pulse sequence diagram.

lines (usually along k_x) are acquired during each RF pulse (in the schematic only one is acquired per RF). Then after a set amount of time after the initial RF pulse, the repetition time (TR), another RF is applied and a slightly lower line (along k_y) of k-space is sampled. After this is repeated several hundred times (depending on the resolution of the image), the entire frequency domain has been sampled and a simple Fourier transform creates the image.

Non-Cartesian k-space Sampling

Radial Sampling

Another fairly common sampling technique is radial. Figure **2.2** shows (a) how radial sampling traverses k-space and (b) a pulse sequence diagram. Similar to Cartesian sampling, a

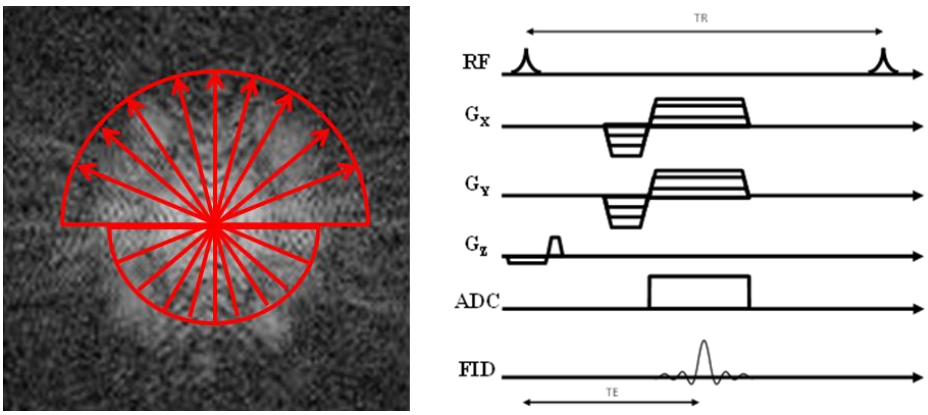

Figure 2.2: Schematic of Radial trajectory. (a) traversing k-space (b) pulse sequence diagram.

small number of lines are acquired during each RF pulse. Consequently, multiple RF pulses are used (separated in time by TR). After several hundred RF pulses, the entire frequency domain is sampled. Unlike Cartesian sampling, however, both k_x and k_y gradients are played while the signal is acquired, and as a result a simple Fourier transform will not yield an image—rather, projection-reconstruction (for more information the reader is referred to (9,10)) or a process called gridding must be used.

Gridding and Alternatives

Non-Cartesian acquisitions require additional steps before an image can be made. The most common technique is called "gridding" which maps the non-Cartesian frequency information onto the Cartesian Fourier domain. One way to think about this is that as the non-Cartesian acquisitions traverse k-space they travel around well-defined k_x and k_y locations. Consequently, in order to use a fast Fourier transform to move from the frequency domain into the image domain, a gridding or an energy dispersion method must be applied to take the sampled frequencies and map them on to the Cartesian frequency domain. For more information, the reader is referred to (11-14).

In our analysis of Oxygen Extraction Fraction (OEF), we found gridding to provide inadequate spatial resolution and consequently, we use an alternative approach—Conjugate Gradient (CG) Minimization, which is discussed in depth later in this work.

Chapter 3 Cerebral Hemodynamic Autoregulation

In the event of damage to the hemodynamic system of the brain, an autoregulatory response is elicited to maintain the supply of blood and oxygen to the tissue. Over the past 20 years, considerable work has been done to understand the brain's auto-regulatory systems and how certain deficiencies may lead to hemodynamic failure. Derdeyn et al. (4,15) used radiolabeled [^{15}O] positron emission tomography (PET) to study the progression of cerebrovascular disease in terms of the "stages" of hemodynamic failure. By quantifying compensatory mechanisms, he found that patients with increased cerebral oxygen extraction fraction (OEF) distal to a carotid artery occlusion, were more likely to have a stroke within the next year. In similar work, Nemoto et al. developed a 3-stage model predicting hemodynamic failure (16). In both models the severity of compromise (i.e., the "stage") is reflected in changes in the cerebral blood volume (CBV), cerebral blood flow (CBF), oxygen extraction fraction (OEF) and cerebrovascular reserve (CVR). Along the same vein, Raichle (17), has shown that one of the first auto-regulatory mechanisms is the dilation of the arteriole bed, which in turn increases CBV. The dilation of the arterioles reduces the vascular resistance which helps maintain blood flow. However, as perfusion pressure continues to fall with disease progression, ultimately CBF will drop—which causes a compensatory increase in oxygen extraction. A schematic of this process is shown in Figure 3.1, taken from Nemoto (16).

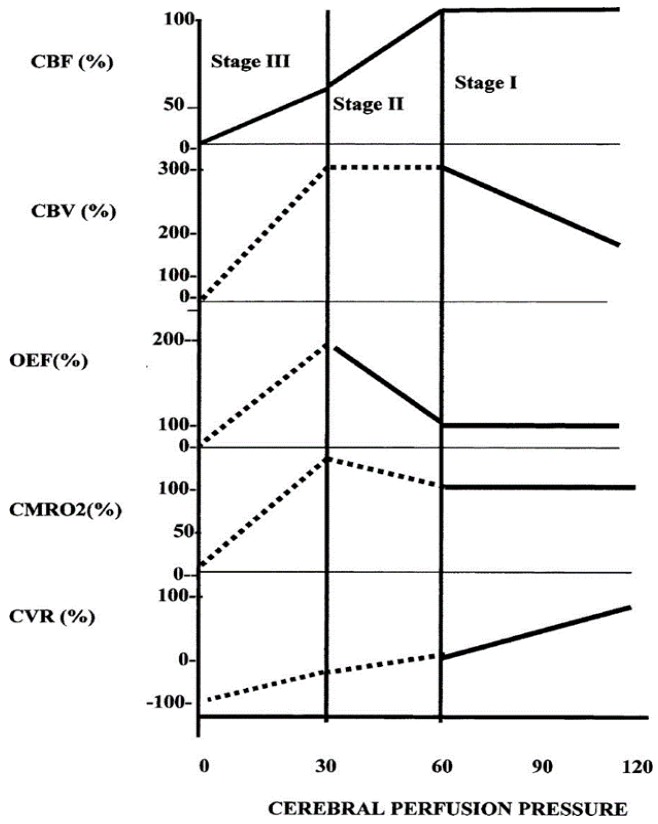

Figure 3.1: Schematic showing progression of hemodynamic compromise.

Significance of OEF and CVR

OEF is a core component of cerebral hemodynamic health and a central contributor to the metabolic consumption rate of oxygen ($CMRO_2$), defined as $CMRO_2 = CBF * C_a * OEF$, where C_a is the concentration of oxygen in the arterial blood. Derdeyn et al. showed that an asymmetric increase in OEF is an *independent indicator of stroke and stroke severity* as well as an *accurate indicator of penumbral volume* (4,15). Furthermore, OEF has been referred to as the "holy grail" of medical imaging because of its importance in the hemodynamic model of the brain. Additionally, a reliable method for imaging CVR is significant as well. As shown in Figure 3.1, CVR varies linear with cerebral perfusion pressure and thus quantifiable CVR can determine

patient disease stage. While there are several ways to clinically image CBV and CBF using MR, the measurements of OEF and CVR are complex and are only available at advanced research centers, with OEF requiring an on-site cyclotron for ^{15}O PET-imaging and CVR requiring multiple perfusion scans (either CT, MRI or PET) and the introduction of a physiologic challenge (for example CO_2 or acetazolamide). One of the primary goals of this work was create imaging techniques for OEF and qCVR that can be used under clinical settings to quantify the patient's risk of future stroke.

Current Techniques: Penumbral Imaging

In many patients, the risk of stroke, if properly identified, can be reduced by treatment with asprin/plavix. For patients who are refractory to medical management and suffer recurrent minor strokes, angioplasty of affected vessels is an option. In all cases, the degree of hemodynamic compromise can guide clinical decisions. Currently, physicians use serveral imaging modalities to assess the severity of the stroke and its potential to recur or grow. The most popular clinical method of examining stroke patients revolves around determining penumbral volume. The penumbra contains at risk tissue and is defined as the region which contains live cells but has reduced oxygen availability, and is thus considered to be "salvagable tissue". Clinically, if there is a large penumbral volume, physicians administer tissue plasminogen activator (tPA). tPA can cause hemorraging in upwards of 15% of patients, however, and is thus used sparingly. Consequently, accurately imaging penumbral volume is extremely important clinically. In most environments, the penumbra is estimated as the perfusion/diffusion mismatch. Currently, this mismatch is defined by regions of elevated Cerebral Blood Flow (CBF) but have no diffusion abnormalities. Recently, however, there have

been several groups questioning the accuracy of this method [19-21], making OEF and qCVR imaging more important than ever.

Chapter 4 Transient Susceptibility Imaging as a Measure of Hemodyanmic Compromise

4.1 Overview

Basic Principles of BOLD imaging and Current Techniques

The Blood Oxygen Level Dependence (BOLD) effect is caused by the magnetic differences between oxygenated hemoglobin (oHb) and deoxygenated hemoglobin (dHb). While oHb is diamagnetic, dHb has 2 unpaired electrons giving it paramagnetic properties. Thus regions with dHb experience a slightly different magnetic field, which causes susceptibility shifts. Hence, measured frequency shifts can be attributed to a change in the ratio of oHb to dHb. This ratio is directly related to the OEF. As oxygen is taken up in the tissue, it is released from the hemoglobin and diffused into the tissue cells.Quantitative BOLD (qBOLD) is a widely researched OEF imaging method taking advantage of the BOLD effect. qBOLD estimates the capillary bed as a series of infinite cylinders oriented uniformly across a magnetic field. With this estimation, Yablonskiy et al (18,19) have created a mathematical approximation for the signal change caused by an oxygenating change in hemoglobin (Equation 15).

$$\boldsymbol{S(t) = e^{\left[(-R_2^t * t) * (DBV * .33) \int_0^1 (2+u)\sqrt{(1-u)} \frac{1-J_0(1.5*\delta\omega*t*u)}{u^2} du\right]}} \quad (15)$$

where $\delta\omega$ varies linearly with OEF, defined as (Equation 16).

$$\boldsymbol{\delta\omega = \frac{4}{3}\gamma\pi\Delta x_0 * Hct * (OEF * B_0)} \quad (16)$$

The mathematical representation in Equation 15 has proven to be challenging to implement in the clinical environment. Certain approximations must be made that don't necessarily hold true in normal volunteers and prove even more problematic in symptomatic

patients with abnormal hemodynamics. Additionally, current qBOLD techniques require a 9 parameter fit, which is both computationally expensive as well as prone to common fitting artifacts/errors (e.g. local minima solutions, noise fitting, etc.). To address these issues, we measure frequency shifts from Equation 16 directly, however, this method has its own challenges.

OEF effects are typically large, affecting a vascular territory or oftentimes an entire hemisphere. The length scales associated with parenchymal OEF, coupled with the near uniformity of normative OEF across the brain (17) dictate the development of an imaging approach that is sensitive to low-spatial frequency imaging behavior. Many current susceptibility imaging approaches have had great success by enhancing high spatial frequency behavior to detail in the veins (20). However, in these techniques require removal or "normalization" of low spatial frequency signal to mitigate air/tissue boundaries in the auditory canals and frontal sinus and other sources of non-uniform local magnetic fields. Consequently, the residual phase resulting from geometric field inhomogeneity has been a challenge for these techniques in clinical translation of OEF imaging. To address this challenge, we have developed scan protocol and post processing algorithm to filter out geometric field inhomogeneity and relax the spatial frequency requirements on susceptibility mapping by filtering through the temporal domain.

Relevance to ICAD and Study Purpose

Intracranial atherosclerotic disease (ICAD) (i.e., the gradual accumulation of cholesterol plaque in the wall of an artery) is considered the leading cause of stroke worldwide. In an autopsy study (n = 3,324), Baker et al (21) showed that the incidence of ICAD is 23% in people between 50-60 years and increases to 80% in people 80 and older, with higher prevalence in

Asian(22), African American and Hispanic populations(23). In symptomatic ICAD with high grade stenoses (70%-99%), the risk of stroke or death within 30 days is 10% in untreated patients.

The prognosis of patients with symptomatic ICAD is poor even with the primary treatment, antiplatlet/antithrombotic medical management, carrying a risk of stroke or death of 6% at 30 days, and 20% at 2 years (24). Although endovascular therapies such as angioplasty/stenting exist (25), they are not used as a primary treatment since they carry a high surgical complication risk. A large (n=451) randomized trial (Stenting versus Aggressive Medical Management for Preventing Recurrent Stroke in Intracranial Stenosis: SAMMPRIS), found the rate of stroke or death of 14% within 30 days (24). Angioplasty/stenting despite the risk, is utilized in the 17% of patients where aspirin/Clodipodgrel fail to prevent neurological decline (26). Given the devastating and costly consequences of stroke in medically treated patients, there is a need for early detection of patients whose auto regulatory capacity is compromised leaving them at the highest risk for stroke recurrence.

Because of the prevalence of ICAD and its association with stroke risk, we imaged 11 consecutive ICAD patients. The purpose of this study is to report on a MRI scan protocol that is sensitive to tissue oxygenation in the brains of hemodynamically compromised patients. We introduce cardiac gating and model the time dependence of signal changes within generalized linear time invariant system theory. Temporal information allows us to directly compare physiologic changes resulting from neurovascular disease without the underlying magnetic field imperfections. We show that cardiac gated susceptibility mapping is sensitive to hemodynamic changes precipitated by neurovascular disease.

4.2 Introduction

Ischemic stroke is the leading cause of long term disability and the 3rd leading cause of death in the industrialized world with approximately 20-30 percent of all strokes originating from intracranial disease (1). Ischemic stroke occurs when a thromboembolus obstructs a blood vessel feeding a specific vascular distribution of the brain reducing the oxygen availability to the surrounding tissue. With the United States' current population aging, the number of individuals at risk for stroke along with the associated health care costs are anticipated to rise considerably in the coming years. Consequently, there is an unmet need to identify patients with cerebrovascular disease who are susceptible to ischemic stroke so that prophylactic medical management may prevent this devastating event.

The benefits of MRI in the acute ischemic stroke setting has been debated with varying results. The Diffusion and Perfusion Imaging Evaluation for Understanding Stroke Evolution II (DEFUSE II) trial demonstrated the benefit of using MRI selection to stratify patients for successful versus unsuccessful interventional therapy (27). However, the Mechanical Retrieval and Recanalization of Stroke Clots Using Embolectomy (MR-RESCUE) clinical trial was unable to conclusively show any benefit of using MRI in the acute stroke setting (28). Subsequently, the randomized controlled EXTEND-IA and SWIFT-PRIME trials confirmed the benefits of CTP and MR DWI-PWI imaging with standardized post-processing selection, demonstrating the significant benefit of mechanical thrombectomy versus IV tPA for large vessel ischemic stroke (29,30). However, the current MRI paradigm of measuring PWI to identify the mismatch or a salvageable penumbra for patient triage is suspect to inconsistency of differentiating oligemic versus ischemic penumbra. We hypothesized that the addition of OEF and transient OEF

measurements will greatly enhance the ability of clinicians to identify the volume of "tissue at risk" in acute ischemic stroke patients as well as in patients with chronic impaired cerebrovascular reserve. The clinical need for a fast, non-invasive imaging method for direct imaging of tissue oxygenation prompted the National Instistute of Health (NIH) and the National Institute of Neurological Disorders and Stroke (NINDS) to recommend researchers "conduct poststroke (acute and chronic) imaging studies to understand cerebral hemodynamics, collateral flow, oxygenation, and brain metabolism effects on tissue" (31).

Our technique differs from previous techniques (19,32-36) by examining frequency fluctuations temporally. While absolute frequency shifts caused by OEF are important, static field inhomogenieties can make it difficult to parse out the useful information. However, by examining temporally spaced images we are able to see through the static "noise" and left with only the dynamic OEF signal.

4.3 Materials and Methods

This investigation was fully HIPAA (Health Insurance Portability and Accountability Act) compliant and was approved by Northwestern University's IRB (Institutional Review Board). All subjects provided written, informed consent.

Theory

Parameter Assessment by Retrevial from Signal Encoding (PARSE)

The PARSE technique (37-39) takes advantage of a longer acquisition window to exacerbate R_2* decay and ω shifts in the signal received by the scanner as described in Equation

$$\boldsymbol{S(t) = \iint M_0(x,y) e^{-\left(R_2^*(x,y) - i\omega(x,y)\right)t} e^{-2\pi i\left(k_x x + k_y y\right)} dxdy} \quad (17)$$

Where M_0 is the initial transverse magnetization at location (x,y), R_2* is the local decay rate and ω is the local frequency, and k_x and k_y are the k-space sampling points. The PARSE acquisition is based on a rosette trajectory (see Figure **4.1**a) to ensure frequent re-sampling of the central k-space data and smooth gradient wave forms to minimize eddy current effects. The rosette k-space trajectory, $k_t = k_f\, cos(\omega_1 t) e(-i\omega_2 t)$, is similar to that of a spiral readout in that both spiral and rosette are characterized by fast oscillating frequency (ω_1) and a slow rotating frequency (ω_2). Based on the constraints of the scanner hardware and the requirement that we re-sample the central k-space region, ω_1 was calculated as 3874.8 Hz and ω_2 was 1610.8 Hz.

From a single echo, S(t), we solve Equation 17 using an inverse estimation technique. To do this we employ an iterative Progressive Length Conjugate Gradient (PLCG) algorithm to estimate M_0, R_2*, and local frequency *offset*, $\delta\omega$, for each pixel location to minimize the residual between the observed signal and estimated signal, $\hat{S}$(t), in a least squares manner (Equation 18).

$$\boldsymbol{Error = \sum_t \left(S(t) - \hat{S}(t)\right)^2} \quad (18)$$

In our algorithm, $\hat{S}$(t) is calculated by placing the estimated M_0, R_2*, and $\delta\omega$ maps into Equation 17. While the conjugate gradient method theoretically produces an exact solution after a finite number of iterations, we found that in practice the problem is ill-posed and estimates of the A-orthogonal vectors were never exact (due to round off error and matrix size) and thus solutions were highly dependent on initial guesses. To address this we employed an iterative PLCG, where our first guess was always a zero estimate. Our algorithm begins by minimizing

error for a signal with 100 data points (encompassing information from TE of 9.6 ms to 9.85 ms). Afterwards, we progressively add data until all information is included (TE of 9.6ms to 80ms), where each iteration uses the solution from the previous step as its initial guess. For each step the conjugate gradient algorithm is stopped when error improvement falls below 5%. Following the initial PLCG we take the M_0, R_2*, and $\delta\omega$ maps, and slightly perturbed them (<1%)—passing the perterbed images as the initial guesses for the following iteration. We have found that this iterative PLCG method provides better estimations in less time than a simple CG method. A schematic of the reconstruction algorithm is shown in Figure **4.1**b, where the CG, PLCG, and iterative PLCG components are represented by the green, blue and red outlines repectively. This technique allows us to produce quantitative M_0, R_2*, and $\delta\omega$ images from a single 80 ms acquisition.

PARSE is well described here (37-41). The primary benefits behind PARSE are the ability to acquire a 2D image set in a single 80 ms readout as well as its high sensitivity to local frequency changes because of the rosette trajectory's re-sampling of the center of k-space. Furthermore, because we collect signal over a long ADC (80 ms), we are able to see phase accrual and R_2* decay over a much longer duration than normal scans where the ADC < 3 ms.

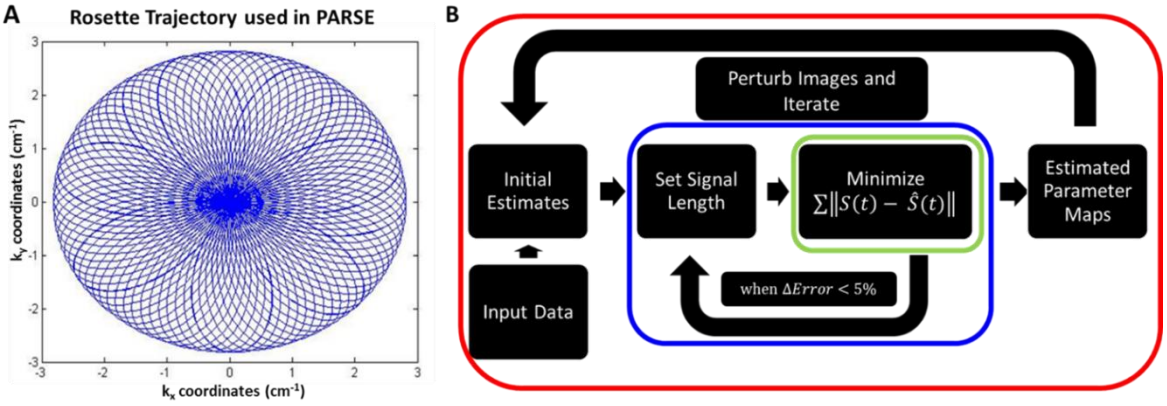

Figure 4.1: OEF Rosette and Reconstruction Schematics. (A) Rosette trajectory used in the PARSE acquisition. (B) Schematic of the iterative PLCG reconstruction algorithm. Green, blue, and red outlines represent the CG, PLCG, and iterative PLCG components respectively.

OEF Calculation

To image OEF using MRI, we take advantage of the blood oxygen level dependence (BOLD) effect. The BOLD effect is caused by a magnetic shift between oxygenated hemoglobin (oHb) and deoxygenated hemoglobin (dHb). While oHb is diamagnetic, dHb has 2 unpaired electrons giving it paramagnetic properties--causing measureable susceptibility differences between the two.

Yablonskiy and others (19,35,36) have described a quantitative approach to estimating the BOLD signal (qBOLD). By modelling the vasculature as a series of infinite cylinders randomly oriented, Yablonskiy has shown the reversible signal relaxation rate (ie. R2') is proportional to the deoxygenated blood volume (DBV) given by (Equation 19)

$$\boldsymbol{R_2' = DBV * \delta\omega} \tag{19}$$

Yablonskiy showed that Equation 19 is relevant for echo times (TE) outside the static dephasing regime—characterized by the critical time, t_c. The rosette trajectory is a multi-echo acquisition and consequently, has many TEs well above t_c. Thus, we ensure OEF is linearly

proportional to δω by only analyzing data outside the static dephasing regime where TE is greater than the calculated critical time t_c (calculated as 9.8ms (42)). Therefore, we can calculate OEF as a function of δω given by:

$$\boldsymbol{\delta\omega = \frac{4}{3}\gamma\pi\Delta x_0 * Hct * (OEF * B_0)} \quad (20)$$

where δω is the deoxyhemoglobin induced frequency shift, $\Delta\chi_0$ is the susceptibility difference between oxygenated and deoxygenated blood, Hct is the hematocrit and B_0 is the magnetic field strength in Tesla. By utilizing PARSE outside of the static dephasing regime, we can directly relate the measured δω to OEF, discussed extensively in (37).

Independent Component Analysis for Removing Static Components

A significant challenge of susceptibility imaging is distinguishing between physiologic specific signal, such as the difference between oHb and dHB, and local field inhomogeneity from air-tissue interfaces such as the frontal sinuses and auditory canals. To address this challenge we estimate and remove static field inhomogeneities using ICA. ICA is well described and widely used across multiple fields (43-45). In short, ICA uses minimization of mutual information to solve, $x=As$, where x is the observed data, A is the estimated mixing matrix, and s is comprised of mutually independent components. In our implementation, x is comprised of 25 temporally separated PARSE Free-Induction Decay (FID) signals. A is composed of the temporal weightings of each of the mutually independent components and s includes the static and dynamic FID components. It is important to note that our implementation of ICA uses raw k-space data and separates components based solely on signal dynamics without regard to anatomic queues which are known to introduce bias when selecting individual components for

further analysis (45). In this way we are blinded to the anatomic distribution of the dynamic signals that we extract.

Cerebrovascular Reserve from δω Images

The progression of intracranial vascular disease has been studied from an imaging perspective through quantifying changes in CBV, CBF, OEF and CVR. Direct physiologic measurements in patients using advanced PET imaging (4,15-17), have shown the earliest imaging changes result from local reduction to vascular resistance and capillary dilation (increased CBV) which maintain CBF and OEF with normal ranges. More severe disease precipitates slightly diminished CBF with normal OEF, whereas the most severe disease results in lower CBV, CBF and increased OEF. Locally increased OEF, in particular, has been shown to be an independent predictor of ischemic stroke (15). Comprehensive evaluation of OEF, CBV, CBF and CVR require radiolabeled tracers, respiration of CO_2 or pharmacological challenges and the injection of an MRI contrast agent. Although CVR evaluation is complex, it is hypothesized that CVR varies linearly throughout the disease progression, making CVR evaluation a desirable imaging metric of the staging of cerebrovascular disease (4,16).

We derive a surrogate for CVR within the system theory by modelling the dynamic intracranial pressure changes resulting from the cardiac cycle and dynamic changes to δω as observables in a linear time-invariant system. Our approach is similar in concept to a 2-element Windkessel model which describes flow, Q(t), and pressure, P(t), in the cardiovascular system as input and output signals to the system, respectively (**4.2**a). In the cerebral vasculature we hypothesis that an exponential impulse response function,

$$\boldsymbol{VRF} \propto \frac{\mathbf{1}}{\boldsymbol{V_r}} \boldsymbol{e}^{-\frac{\boldsymbol{t}}{\boldsymbol{V_r C}}} \tag{21}$$

where V_r is the vascular resistance of the brain and C_v is the vascular compliance, characterizes the system (Derived in Appendix A).

Here we introduce the vascular residue function (VRF), which is modelled as an exponential decay dependent on arteriole resistance and compliance. As our measurements are taken during diastole, we would expect to see an exponential decay with time as the arterioles flush oxygenated blood towards the capillary bed.

It is important to note that while the venous flow may remain relatively constant throughout the cardiac cycle, the pulsatility within the arteriole bed is of interest. As the pressure waveform travels to the arterioles, the amount of oxygenated blood will increase resulting in a relative decrease in dHb in that area's blood vessel (similar to fMRI). It is hypothesized that in a diseased state, the local blood transit time differs significantly affecting the oxygenated to deoxygenated blood ratio.

Healthy vs Compromised

Raichle (17), has shown that as cerebral vasculature is compromised a series of compensatory effects begin to take place. This auto-regulation helps preserve nutrient and oxygen supply to the brain during any type of hemodynamic compromise. One of the first auto-regulatory mechanisms is the dilation of the arteriole bed, which in turn increases CBV. In our Windkessel model, this dilation of arterioles simultaneously decreases vascular resistance (V_r) and compliance (C). Figure **4.2**b shows a schematic of what might happen distal to a stenosis in a compromised vessel.

Data Acquisition

MRI-based OEF and reactivity scans were acquired under a number of physiologic conditions (breath-hold challenge and neurovascular disease). We post processed images and compared pre/post challenge images in the case of healthy normal and interhemispheric values in pathology to determine the level to which dynamic images of OEF reflect different physiologic states. In this pilot study of a new technique, we hypothesized that the decrease in resistance and compliance alters (shortens) the vascular residue function (VRF), shown in Figure **4.2**d, and should be measureable with high enough temporal resolution.

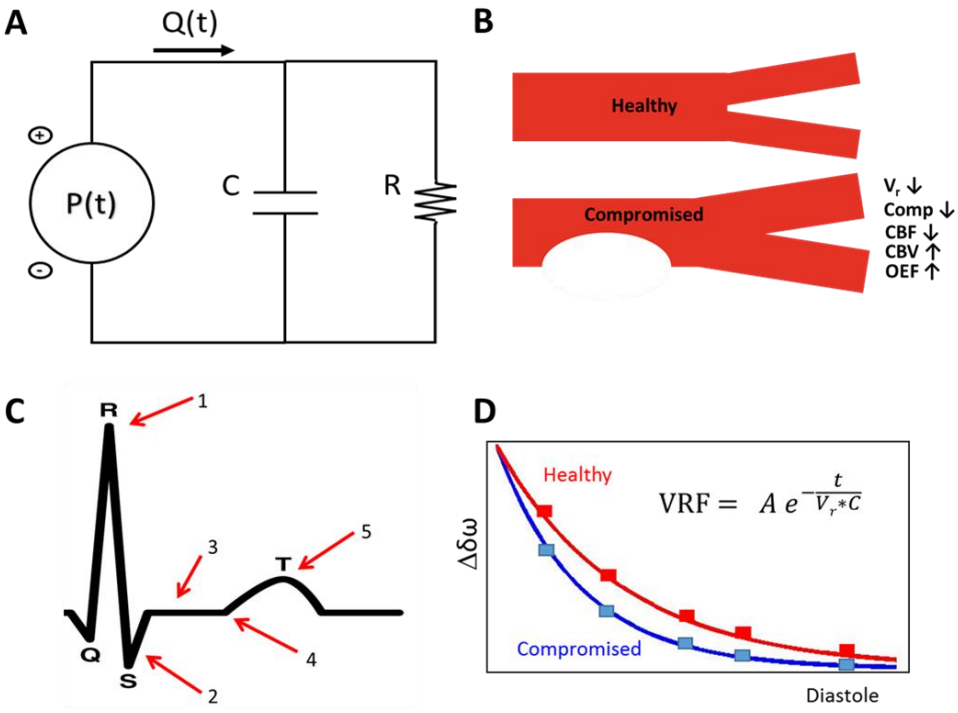

Figure 4.2: Schematic of Windkessel Model. (A) Schematic of the Windkessel model with downstream compliance, C, and resistance, R. (B) Schematic of vasculature affects distal to a stenosis. In compromised vasculature, we expect to see reduced vascular resistance and reduced compliance. This will result in increased CBV, decreased CBF, and increased OEF to compensate. (C) Schematic showing cardiac gated acquisitions. Rosettes FIDs are taken in 25 ms increments after the R-wave. (D) Proposed vascular residual function (VRF). Note that compromised tissue should have a faster decay coefficient.

Hypercapnia Volunteer Study

To examine the ability of ICA-PARSE to measure transient susceptibility fluctuations, we scanned 4 healthy individuals under mild hypercapnia induced by a 25 second breath-hold. A series of 20 rosette acquisitions was taken twice on each volunteer. During the first series acquisition the volunteer was instructed to exhale and hold their breath for 25 seconds. During the following series the volunteer underwent normal breathing. ICA was performed on the resulting time-courses.

To determine proper thresholding, we examined a range of cutoff values for dynamic component classification. To calculate the component baseline mean, outliers (more than 2 standard deviations from mean) were removed and then the mean of the first 7 time points was taken. Dynamic components were classified as a deviation of more than between 0.1 and 2.5 standard deviations from the baseline mean during the breath-hold. The optimal cutoff value was determined as the most statistically significant difference in the number of dynamic components between breath hold and non-breath-hold time series, while still allowing for more than 2 dynamic components on average.

Cardiac Gated Patient Protocol

All patients enrolled in our study were scanned on 3T MR scanner (Skyra Siemens Medical Solutions, Malvern, PA). Data was collected on 11 patients (M/F 5/6, <age> = 52.1 ± 11.1). We acquired a single slice, 5.0 mm thick, 210 mm x 210 mm FOV, 108 x 108 matrix, resolution = 1.94 x 1.94 x 5 mm^3 2D PARSE images, with the acquired slice placed approximated 5mm above the ventricles. The sequence was cardiac gated where each slice was acquired 25 times, at 25 ms increments from the R-trigger throughout the cardiac cycle (25ms to

625ms delay), see Figure **4.2**c. To allow complete longitudinal signal regrowth the repetition time (TR) was 5 secs. Total scan time was approximately 2 minutes. Four patients had clinically available perfusion sequences.

Patient Recruitment

Institutional review board approval was obtained for a prospective, HIPAA compliant study of symptomatic patients presenting with ischemic stroke or transient ischemic attack (TIA), secondary to intracranial atherosclerotic disease (ICAD) with >50% stenosis and plaques involving the internal carotid artery (ICA), A1-A2 anterior cerebral, M1-M2 middle cerebral, and P1-P2 posterior cerebral arteries (ACA, MCA, PCA) or basilar artery (BA) – see Table 1. Patients were identified and recruited for this study at our institution from March 2013 to May 2015, after receiving a standard clinical head and neck MRI/MRA evaluation including 3D TOF. Patients were consented based upon a willingness to participate in a longitudinal study and ability to undergo a research MRI examination within 30 days of the ischemic event.

Post Processing

PARSE readouts were acquired separated by $\Delta t = 25$ms from the onset of the R-wave during the cardiac cycle. Prior to image reconstruction ICA was performed on the time-series of Free Induction Decay (FID) data to extract and decompose the data into dynamic components. Components that fluctuated by more than 1.6 standard deviations (discussed in results) throughout the cardiac cycle were used to reconstruct the dynamic FID signal allowing us to create a signal no longer containing static components. For cardiac gating the baseline mean measurements were measured from the end of the time series (when the patient was well into diastole). The dynamic FIDs were then used to reconstruct a series of images temporally

separated by 25ms. The local frequency time series of images δω(t) were used in the statistical testing and modelling.

Image Reconstruction

The PARSE k-space data were exported, reconstructed and post-processed offline using software developed in house using MATLAB (v 12.0, Mathworks, Natick, MA). PARSE image reconstruction uses an iterative progressive length conjugate gradient, non-linear least squares algorithm that extracts M_0, R_2* and local frequency offset (δω) from the 80 ms acquisition. Baseline OEF values were calculated using Equation 4, taking advantage of the linear relationship between δω and OEF. Similar to previous studies we assumed a constant HcT value of 18 ppm. Whole brain hemispheric ROIs were automatically drawn and regions immediately surrounding the frontal sinuses removed.

CVR modelling

For each pixel of the ICA'd frequency images, baseline δω was measured as the mean of the final 4 time points. The deviation from baseline was then fit to an exponential decay function of the form given by Equation 22,

$$\boldsymbol{\Delta\delta\omega(t) = Ae^{-\beta t}} \tag{22}$$

where according to Equation 21, β should be proportional to the inverse of vascular resistance and compliance. Consequently, the β is used as a surrogate for hemodynamic compromise, where a faster return to baseline (or a larger β) correlates with the local VRF. For imaging purposes, the inverse of β was used as a surrogate for rCVR.

Statistical Analysis

Breath-Hold Analysis:

The number of dynamic components were compared between breath-hold and non-breath-hold time series. The optimal cutoff value was determined as the most statistically significant difference in the number of dynamic components between breath hold and non-breath-hold time series, while still allowing for more than 2 dynamic components on average.

Hemispheric Indices:

To remove the bias associated with ROI drawing, we employed an automated hemispheric algorithm. ROIs were created using non-ICA'd M_0 images. First, a whole brain mask was generated—defined as .7 standard deviations above image mean. With the whole brain ROI, the center of mass was generated and was then bisected using a perceptron algorithm to separate right and left hemisphere masks. Mean values of OEF and β were calculated for affected and healthy hemispheres and a paired Student's t-test used to test the hypothesis that elevated hemispheric OEF and β occur in the impaired portion of the brain. For transient OEF, hemispheric values were calculated as the percentage of energy on the affected and healthy sides. Significance was defined as <0.05 in all statistical tests.

4.4 Results

Figure **4.3** a and b show the results from the volunteer breath-hold study. Notice that the number of dynamic components as measured via ICA is always greater during the breath-hold task. From this analysis it was determined that a fluctuation of 1.6 standard deviations ($p < 1.74e-10$) from baseline was optimal. While a cutoff of 1.85 standard deviations had a slightly more significant p value ($p < 8.21e-14$), it did not produce more than 2 dynamic components on

average. Figure **4.3**b shows a representative sample of component time series. The red line denotes the time of the breath-hold.

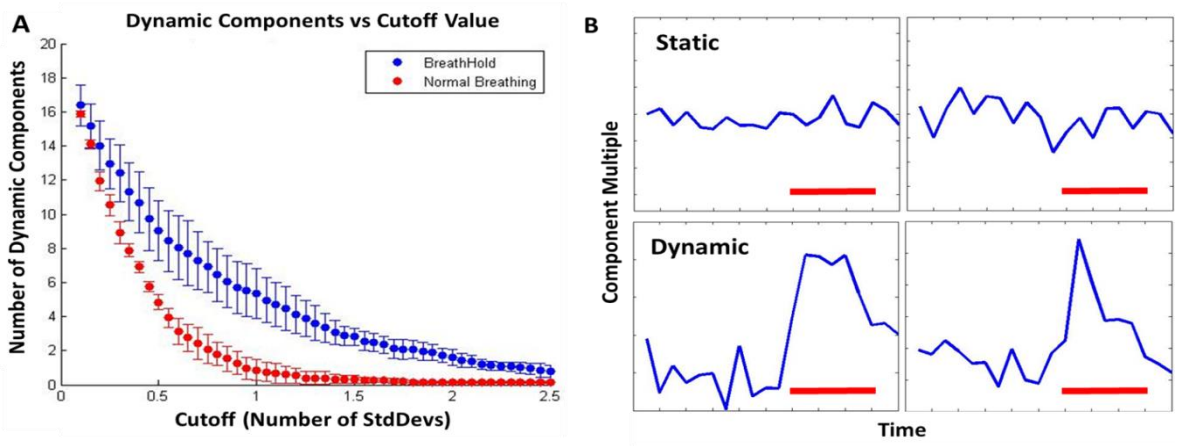

Figure 4.3 ICA cutoff analysis. (A) Graph showing the number of dynamic components automatically generated based on the ICA cutoff values. Note, as expected, the number of dynamic components is always larger for breath-hold data. Based on this result we used a cutoff of 1.6 standard deviations in the cardiac gated study. (B) Representative time-courses of static and dynamic components. The red bar represents the known period of breath-hold.

Figure **4.4** shows an example of pre and post ICA images. Figure **4.4**a-b show images from a healthy volunteer during the breath-hold task. Figure **4.4**c-d show images from a patient with a right ICA stenosis for several times following the R-wave trigger. For both **4.4** a and c, notice the pre-ICA images show little to no temporal fluctuation; the ICA images (b and d), however, show easily identifiable temporal perturbations. In Figure **4.4**b, notice the large increase in BOLD signal toward the anterior portion of the brain. While it is known that a breath-hold causes hyper-capnea that can be seen during BOLD imaging, it is difficult to know for sure what is causing the increase signal seen during breath-hold. In Figure **4.4**d, notice the

early flush and subsequent flow out of signal, showing sensitivity to intra-arterial pressure waveform.

Across the 11 patients, average frequency change across the head was 23.35 ± 5.73 Hz which correlates to an average OEF of 48.63 ± 11.92 %. Our previous work showed 11 control subjects gave a frequency change of 17.6 ± 3.75 Hz corresponding to an average whole brain-slice OEF of 36.66 ± 7.82%, displaying excellent with normative PET literature values.

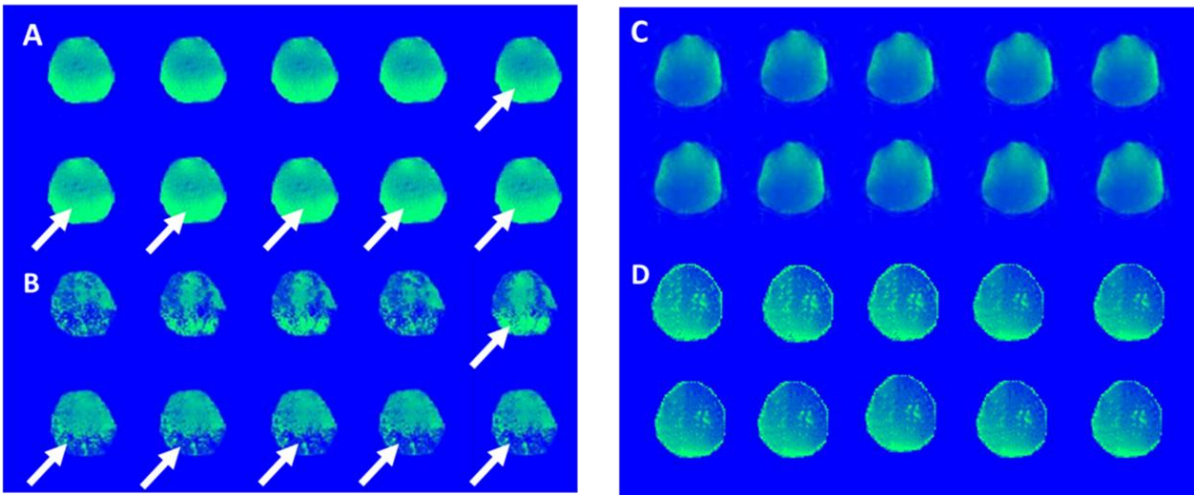

Figure 4.4 Representative OEF images before and after ICA. (A, B) Breath-Hold. Arrows represent time of breath-hold. (C-D) Cardiac-gated from patient with a right ICA stenosis. (A) and (C) show pre-ICA images, with (B) and (D) post-ICA. Notice the pre-ICA images show little to no temporal fluctuation, however, post-ICA images show easily identifiable temporal perturbations.

Table 2 shows calculated mean hemispheric OEF, transient OEF and β values for each patient. Table 2 also shows symptomatic side of the angiographically confirmed stenosis location.

Table 2: Relevant patient information alongside baseline OEF, transient OEF, and β values.

Gender	Age	Stenosis Location	Baseline OEF – Affected Side (%)	Baseline OEF – Unaffected Side (%)	Transient OEF – Affected Side (arb.)	Transient OEF – Unaffected Side (arb.)	Beta – Affected Side ($10^{-3}ms^{-1}$)	Beta – Unaffected Side ($10^{-3}ms^{-1}$)
F	49	R M1 & A1	43.78	42.66	0.71	0.29	9.51	6.44
M	70	R MCA M2	60.09	47.62	0.51	0.49	9.96	9.80
M	45	R MCA M1	40.26	27.37	0.62	0.38	12.35	10.73
F	54	R ICA	58.78	59.36	0.47	0.53	8.68	7.44
F	62	L MCA M2	24.37	24.79	0.53	0.47	9.64	9.68
M	34	L VA	36.43	33.12	0.55	0.45	9.92	9.12
M	66	R M2 & VA	59.36	56.03	0.52	0.48	7.64	7.60
F	59	R A1	59.78	56.34	0.52	0.48	8.16	9.36
F	43	R ICA	65.61	57.07	0.54	0.46	21.05	19.96
M	54	L VA & MCA	48.95	54.70	0.65	0.35	10.60	6.80
F	37	R A2	56.32	57.16	0.52	0.48	10.44	9.68
	52.09 ±11.13		50.34 ±12.13	46.93 ± 12.34	0.56 ±0.067	0.44 ±0 .067	10.72 ± 3.48	9.69 ± 3.51

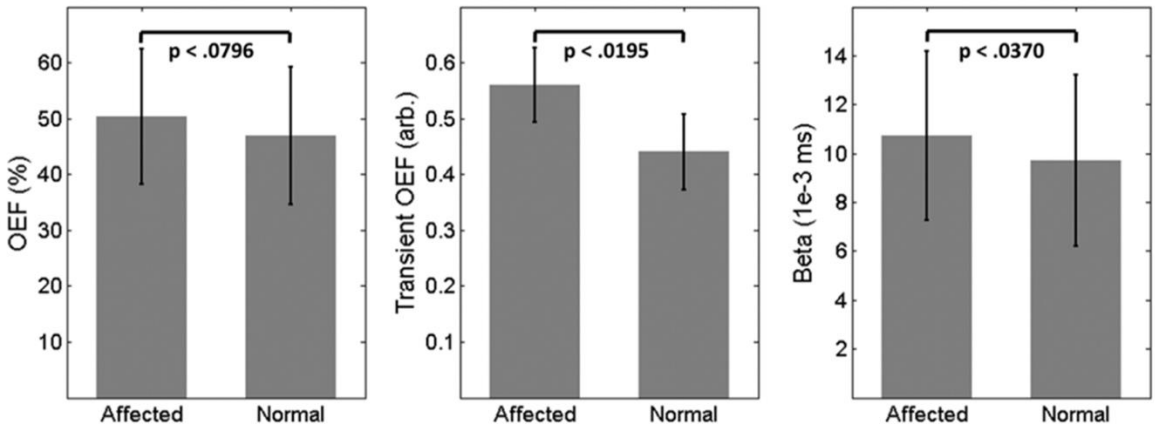

Figure 4.5: Mean hemispheric OEF, transient OEF, and β values. Mean hemispheric OEF, transient OEF, and β values for the 11 patients imaged. Both transient OEF and β show significance. Error bars represent standard deviations.

Figure **4.5** shows mean hemispheric OEF, transient OEF, and β values for the 11 patients imaged. Hemispheric OEF was elevated on the affected hemisphere (50.34 ± 12.13 % vs 46.93 ± 12.34 %), but failed to reach significance ($p < .0796$). Transient OEF showed greater distinction between healthy and compromised tissue (0.56 ± 0.067 vs 0.44 ± 0.067 arb.) with a significant p value ($p < .0195$). β values showed additional information, with hemispheric significance ($10.72 \pm 3.48\ 10^{-3}ms^{-1}$, $9.69 \pm 3.51\ 10^{-3}ms^{-1}$; $p < .037$).

Figure **4.6** shows the results of our study in two representative patients, with each row representing data collected from different patients. Figure **4.6**(a,f) are clinically acquired CBF slices corresponding to the MR-PARSE acquisition slice. Figure **4.6**(b,g) are the corresponding Mean Transit Time (MTT) images. Please note, that for Patient 1, MR-Perfusion was performed while Patient 2 had CT-Perfusion. Figure **4.6**(c,h) are the representative frequency offset images, windowed and leveled to clearly show the frontal sinus interference . Figure **4.6**(d, i) are the frequency offset images after ICA, and (e,j) are relative CVR maps generated by taking the inverse of β from the Windkessel model. For the patients shown, the transient OEF scores were 0.71/0.29 and 0.52/0.48 (Affected vs Healthy), respectively. In patient 1, the hemispheric asymmetry is most clearly seen in the pre-ICA images but easily discerned post-ICA.

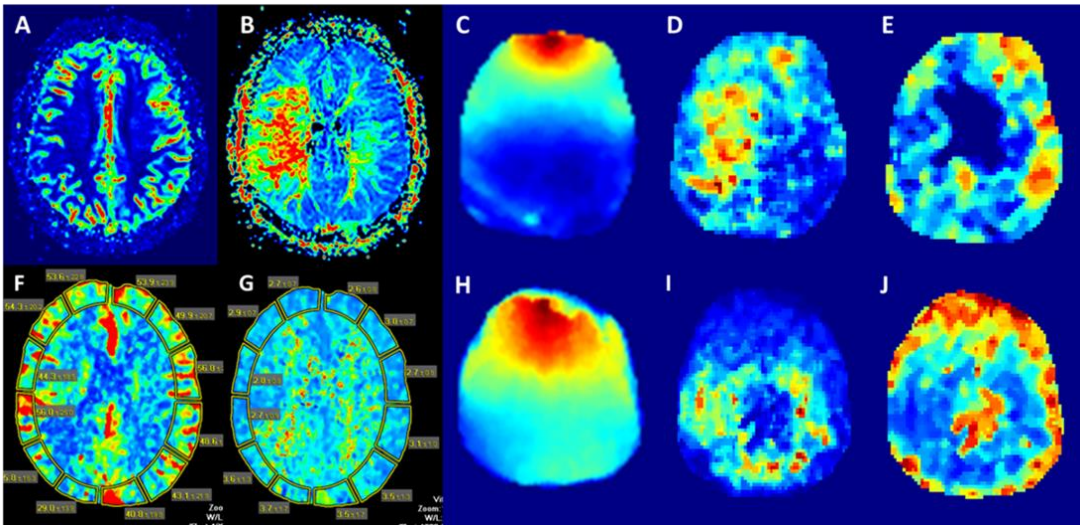

Figure 4.6 Representative OEF images, generated for 2 patients. The top row shows results for a patient with a right M1 stenosis, while the bottom row shows results for a right A2 stenosis. Notice that in the first patient, the CBF is mildly reduced and the MTT is markedly prolonged in the right MCA territory and subsequently exhibits increased transient OEF in that region, while the bottom patient shows largely symmetrical results, with little difference between affected and healthy sides. (A, F) Clinically acquired CBF. (B, G) Mean Transit Time (MTT). (C, H) Frequency offset images, $\delta\omega$, window/level was chosen to clearly show the frontal sinus interference (D, I) Transient OEF Images. (E, J) Relative CVR maps generated by taking the inverse of β from the Windkessel model. For the patients shown, the transient OEF scores were 0.71/0.29 and 0.52/0.48 (Affected vs Healthy), for the top and bottom rows, respectively.

4.5 Discussion

We found that dynamic signal analysis of $\delta\omega$ images improve the detection of hemodynamic compromise in patients with confirmed ICAD. By modeling physiologic signals acquired with MRI within the context of an LTI system we have proposed a new method of measuring rCVR.

The proposed transient PARSE MR-OEF technique has many unique advantages over available PET methods. First, MR is relatively inexpensive when compared to PET counterparts. Secondly, the proposed method could easily be added to current MR stroke protocols. Third, this

technique is non-invasive and easily implemented on currently available hardware across multiple platforms. And finally, MR is much more accessible than PET, especially OEF as PET-OEF requires an on-site cyclotron due to the short half-life of [^{15}O] water label.

While previous work has found that direct measurement of local frequency changes with PARSE agree with physiologic expectations measured by PET, static MR-PARSE is not without its limitations. Background static field inhomogeneities have the potential to be measured as local frequency shifts—artificially elevating OEF values. Previous work has largely relied on shimming techniques to minimize these effects. However, variations in vendor shimming subtleties, focal deposition of iron, and patient air-tissue variations surrounding the sinuses can cause incorrect static OEF measurements. We have sought to address these issues in a novel way—by looking for temporal fluctuations and thus seeing through any static affect that may shift the BOLD signal.

Our initial studies attempted to use breath-hold measurements to gain temporal "task" measurements. However, we failed to see how such a technique would be used clinically. First, hyper-capnea should affect the BOLD signal uniformly, regardless of the underlying hemodynamic compromise. Second, breath-hold tasks are complicated by patient ability and head motion. Figure 4 shows a dramatic change in frequency offset, however, this change may be caused by head-motion resulting in the new slice being slightly closer to the frontal sinus—and the air-tissue interface causing a frequency offset that aligns temporally with the breath-hold. Even beyond patient motion, breath hold tasks are notoriously difficult for hemodynamically compromised patients to perform. It is for these reasons we switched to a cardiac-gated PARSE acquisition. Figure **4.4** shows very clearly, however, that the proposed ICA methodology

removes the static components. While Figures **4.4**a and c show clear static sinus and earhole inhomogeneity, Figures **4.4**b and d do not.

The proposed Windkessel model was developed to model changes in the BOLD signal that might be measured throughout the cardiac cycle. One major assumption in developing the model is that our measurement takes place after the arrival of the pressure wave form. Our first acquisition begins 25 ms after the R-wave trigger. With a 25 ms plus gradient delay and image averaging over 80 ms, we estimate our first temporal image to occur at roughly 60 to 75 ms, after the R-wave trigger. Given the pressure wave velocity of roughly .5 cm/ms and a relatively direct shot from the aorta toward the brain, we'd expect the pressure wave to reach the brain between 30 and 60 ms after the R-wave.

The arrival of the pressure wave will move blood into the arteriole bed. The pulsatility of arteries and arterioles is well documented and can further be visualized by the flow of CSF out of the brain to offset increased volume. In a hemodynamically compromised patient the vasculature auto-regulates (reducing resistance) to help maintain blood flow (and thus, oxygen and nutrients) to tissue. We provide evidence to suggest that in a diseased state, with the vascular resistance reduced, the blood transit time is, as well, reduced. The presented results suggest the proposed method, with temporal resolution of 25 ms, is suitably able to measure these temporal variations.

It is well documented by Raichle, Derdeyn and others, that hemodynamic stress affects perfusion parameters(4,15-17). They have shown that patients entering stage II of hemodynamic failure would exhibit increased CBV, decreased CBF and elevated OEF. Most of the patients examined in our study were symptomatic, and we hypothesize that we are measuring affects around stage II of hemodynamic failure.

Limitations

Several limitations were identified in this study. First and foremost, as can be seen in Figures **4.4** and **4.6**, the spatial resolution as defined by the point spread function for the PARSE method is poor when compared to anatomic or perfusion imaging. We felt, however, that in order to see the VRF during the cardiac cycle, that acquisition speed was paramount. With this in mind we utilized PARSE--both proton density and phase information for a complete slice can be acquired in 80 ms. This temporal speed allowed us to cardiac-gate images and still create a sequence with clinically acceptable table time (<2 minutes). It is also important to note here that Derdeyn showed hemispheric OEF differences predicted stroke risk; and thus, for the proposed use as a predictor of stroke risk, low resolution is more than adequate. We are exploring methods to improve resolution of the image, and this is an active area of research within our group. We were also limited by a rather small sample size (n = 11), as well as data being collected from a single center—exposing us to biases in patient population. In future studies we hope to include more patients and follow them longitudinally as their diseases progress.

4.6 Conclusion

In this pilot study, we present the first evidence of an MR-based OEF and CVR technique that requires no contrast. We have found that MR-PARSE has detectable sensitivity to frequency shifts induced by transient alterations in de-oxyhemoglobin through the cardiac cycle in ICAD patients with greater than 50% stenosis. Furthermore, we have shown that through the use of ICA, transient OEF and β are significant predictors of hemispheric compromise. Our approach to quantify transient BOLD fluctuations due to cerebrovascular reactivity represents a new and simple, non-contrast approach to stratifying patients toward therapies to prevent stroke.

Chapter 5 Validation of Quantitative Cerebral Vascular Reserve using MRI

5.1 Overview

Basic Principles MR-Perfusion

In dynamic susceptibility contrast (DSC) – MRI an intravascular contrast agent is injected into the blood and monitored as it passes through the vasculature. The contrast agent causes susceptibility differences between the blood and surrounding tissue. By analyzing the tracer kinetics during the first pass, one can compute cerebral blood flow (CBF), cerebral blood volume (CBV), and mean transit time (MTT). These measures are clinically useful in the assessment of hemodynamic compromise as well as tumor angiogenesis and a host of other neurovascular diseases.

The most common tracer used is gadolinium (Gd). Within the brain, the blood brain barrier ensures Gd remains within the vasculature. As a result, the high concentration of Gd in the microvasculature creates susceptibility interfaces which result in signal dephasing causing T_2-shortening and ultimately signal loss. It has been shown, that the T_2 relaxation rate varies linearly with the Gd tissue concentration Equation 23

$$\Delta \boldsymbol{R_2(t)} \propto \boldsymbol{C_t(t)} \tag{23}$$

Because of the linear relationship between T2 and contrast concentration, cerebral perfusion images are T_2^* -weighted. One common method is to employ a T_2^* -weighted gradient echo sequence, which has a signal equation given by Equation 24,

$$S(t) = S(t_0)\left[1 - e^{-\frac{TR}{T_1(t)}}\right] e^{-\frac{TE}{T_2(t)}} \quad (24)$$

where $S(t_0)$ is the baseline signal and TE and TR the echo and repetition times. Notice that the longitudinal and transverse relaxation rates are shown as a function of time—as they both shorten with contrast concentration changes. In perfusion sequences, TR is approximately 50 times longer than TE, as a result the signal enhancement caused by T_1 shortening is overwhelmed by T_2 effects. Consequently, the T_1 term can be dropped from Equation 24, and we can estimate Gd concentration as a function signal Equation 25,

$$C_t(t) = -k \cdot \log \frac{\frac{S(t)}{S(t_0)}}{TE} \quad (25)$$

where k is the linear constant relating concentration to T2. By using the above equation, one can determine contrast concentration during the first pass simply by measuring signal intensity. Consequently, by imaging through time, concentration time curves can be measured and tracer kinetics determined. In perfusion imaging, the contrast bolus is modeled as

$$C_t(t) = AIF(t) \otimes h(t) \quad (26)$$

where AIF is the arterial input function and h(t) is the transport function—which describes the probability distribution function of the transit times through the voxel. In MR, C_t and AIF are measured and transport function is determined by deconvolution. In turn, CBF, CBV and MTT are calculated using Equations 27 through 29.

$$CBF = \max\big(h(t)\big) \quad (27)$$

$$\boldsymbol{CBV} = \frac{\int \boldsymbol{C_t(\tau)dt}}{\int \boldsymbol{AIF(\tau)dt}} \tag{28}$$

$$\boldsymbol{MTT} = \frac{\boldsymbol{CBV}}{\boldsymbol{CBF}} \tag{29}$$

Importance of CVR

In the event of damage to the hemodynamic system of the brain, an autoregulatory response is elicited to maintain the supply of blood and oxygen to the tissue. By quantitatively measuring the magnitude of the autoregulatory response, the severity of the hemodynamic impairment can be defined. In this study, we propose a method of accurately measuring quantitative cerebrovascular reserve, which has been hypothesized to vary linearly with cerebral perfusion pressure. We propose a technique for serial quantitative measurements of CBF and validate this in both human and canine models. Finally, we show that qCVR can clearly distinguish between stages of hemodynamic compromise in patients with occulusive vessel disease.

5.2 Introduction

Viability of brain tissue is dependent on the ability of the vasculature to provide ample oxygen and nutrients. In patients with chronic cerebrovascular disease, the ability to maintain blood flow (and thus oxygen and nutrients), is diminished. In an attempt to maintain nutrient supply, the brain has several auto-regulatory pathways. The initial response (autoregulatory vasodilation) reduces vascular resistance to maintain blood flow. As cerebral perfusion pressure (CPP) continues to drop, the reduction in vascular resistance is no longer sufficient to maintain blood flow. With the reduction in blood flow, the tissue is forced to remove more from the

passing blood (increase oxygen extraction). This juncture of decrease blood flow and increased extraction is often referred to as “misery perfusion” (46).

The progression of intracranial vascular disease has been studied from an imaging perspective through quantifying changes in CBV, CBF, OEF and CVR. Direct physiologic measurements in patients using advanced PET imaging (4,15-17), have shown the earliest imaging changes (Stage I) result from local reduction to vascular resistance and capillary dilation (increased CBV) which maintain CBF and OEF within normal ranges. More severe disease precipitates elevated CBF with normal OEF (Stage II), whereas the most severe disease results in lower CBV, CBF and increased OEF (Stage III). Previous to this body of work, comprehensive quantifiable evaluation of OEF and CVR could only be performed using radio labelled PET tracers. Although CVR evaluation is complex, it is hypothesized that it varies linearly throughout the disease progression, making widely available quantification of CVR a desirable imaging metric for cerebrovascular disease staging (4,16).

In this study, we develop a method to accurately quantitate CVR using current MRI-protocols. We show that the use of a WCF specific to the second injection allows for accurate quantification of CBF and validate this in both human and canine models. Finally, we show that qCVR can clearly distinguish between stages of hemodynamic compromise in patients with angiographically confirmed occulusive vessel disease.

5.3 Methods

First, we performed back to back perfusion scans on a cohort of 10 volunteers, to examine the effect of a second injection on perfusion quantification. We then compared MR-qCVR in canines against the perfusion gold standard—microspheres. Finally, we performed an

IRB approved, retrospective review of patients undergoing an MRI perfusion with ACZ challenge exam at our institution. In each case, perfusion was quantified using a previously reported DSC-MRI pulse sequence (SCALE-PWI (47-49)). **Volunteer Study:** To examine the effects of a second injection of gadolinium, ten volunteers were imaged twice using a quantitative DSC perfusion MRI (SCALE-PWI). A different water correction factor was fit using the ratio of T1s for the first and second injection. **Canine Experiment:** Following successful demonstration of quantitative perfusion values for both first and second injections, a canine experiment was performed to compare MR-qCBF and MR-qCVR values against microspheres. 5 canines were examined under resting state and CO_2 elevation. **Patient Data:** A series of sixteen consecutive patients with angiographically confirmed cerebral vascular disease who underwent an ACZ challenge MRI perfusion study as part of their standard of care were retrospectively selected. Cerebral perfusion was quantified using a previously reported DSC perfusion MRI pulse sequence (SCALE-PWI[47-49]). The stage of hemodynamic compromise for each patient was examined.

Theory

It has been shown that steady state CBV (CBV_{SS}) [48], measured by parenchymal T_1 changes (before and post T_1 shortening contrast injections) normalized to blood, will predictably underestimate true blood volume due to intra-to-extravascular water exchange[48,50,51]. Previous work has shown that CBV_{SS} in white matter (WM) can be adequately measured as a ratio of T_1 changes (Equation 30, evaluated in %) and thus quantified CBV_{WM} can be given by Equation 31 [48,49].

$$\boldsymbol{CBV_{SSWM}} = \frac{\left(\frac{\mathbf{1}}{\boldsymbol{T_1^{Post}}} - \frac{\mathbf{1}}{\boldsymbol{T_1^{Pre}}}\right)_{\boldsymbol{WM}}}{\left(\frac{\mathbf{1}}{\boldsymbol{T_1^{Post}}} - \frac{\mathbf{1}}{\boldsymbol{T_1^{Pre}}}\right)_{\boldsymbol{Blood}}} * \mathbf{100} \tag{30}$$

$$\boldsymbol{qCBV_{WM}} = \mathbf{WCF}\left(\boldsymbol{\Delta R_{1,Blood}}\right) * \frac{\mathbf{(1 - Hct_{LV})}}{\boldsymbol{\rho}\mathbf{(1 - Hct_{SV})}} * \boldsymbol{CBV_{SSWM}} \tag{31}$$

where WCF is the water correction factor, ρ is average brain voxel density and Hct_{LV} and Hct_{SV} are the hematocrit levels in large and small vessels, respectively. The WCF fit to empirical data, for each injection, as a function of blood ΔR_1 and is defined by Equation 32.

$$\mathbf{WCF}\left(\boldsymbol{\Delta R_{1,Blood}}\right) = \boldsymbol{A}\left(\boldsymbol{\Delta R_{1,Blood}^2}\right) + \boldsymbol{B}\left(\boldsymbol{\Delta R_{1,Blood}}\right) + \boldsymbol{C} \tag{32}$$

Once $qCBV_{WM}$ is determined, whole brain qCBV and qCBF are calculated using the ratio of quantitative to relative values as shown in Equations (33 through 36). To account for vasodilation or vasoconstriction, second injection calculations include the ratio of steady state CBV between first and second injections. Subscript numbers represent injection number.

$$\boldsymbol{qCBV_1} = \boldsymbol{rCBV_1} * \frac{\boldsymbol{qCBV_{WM,1}}}{\boldsymbol{rCBV_{WM,1}}} \tag{33}$$

$$\boldsymbol{qCBF_1} = \boldsymbol{rCBF_1} * \frac{\boldsymbol{qCBV_{WM,1}}}{\boldsymbol{rCBV_{WM,1}}} \tag{34}$$

$$\boldsymbol{qCBV_2} = \boldsymbol{rCBV_2} * \frac{\boldsymbol{qCBV_{WM,2}}}{\boldsymbol{rCBV_{WM,2}}} * \frac{\boldsymbol{CBV_{SSWM,2}}}{\boldsymbol{CBV_{SSWM,1}}} \tag{35}$$

$$\boldsymbol{qCBF_2} = \boldsymbol{rCBF_2} * \frac{\boldsymbol{qCBV_{WM,2}}}{\boldsymbol{rCBV_{WM,2}}} * \frac{\boldsymbol{CBV_{SSWM,2}}}{\boldsymbol{CBV_{SSWM,1}}} \tag{36}$$

CVR is then calculated a ratio of qCBF values taken before and after a vascular challenge. In the case of humans the challenge was an injection of Acetazolomide, while for canines increased CO_2 was used. In both cases, quantitative CVR measurements (in %) were calculated using Equation 37.

$$qCVR = \frac{qCBF_{Post-Challenge} - qCBF_{Baseline}}{qCBF_{Baseline}} * 100 \quad (37)$$

Validation of Quantification in Multiple Injections: Volunteer Data

To examine the effects of a second injection of gadolinium on measured quantitative perfusion values, ten volunteers were imaged twice using a quantitative DSC perfusion MRI (SCALE-PWI [47-49]). One volunteer was removed from analysis due to a failed second injection. All patients were imaged back to back using a 1.5T (Espree, Siemens) MR scanner with the following parameters: TR/TE = 1,090/34 msec, matrix size = 128 x 128, FOV = 220 mm x 220 mm, for an in-plane resolution of 1.72 mm, flip angle = 20°, Slice thickness = 5 mm, acceleration factor = 2, with 13 slices. Total perfusion scan time was 1 minute 47 seconds. A single dose injection (0.1 mmol/kg body weight) of Gd-DTPA (Magnevist Berlex, Princeton, NJ) was followed by a 15 mL saline flush, at 4 mL/s. The second DSC-MRI scan was taken five minutes after the completion of the first using the same parameters described above. It is important to note, that volunteers did not undergo any physiologic challenge.

A different water correction factor was fit as a function of blood ΔR_1 using the T_1 values from the first and second injections separately. For each injection, whole brain qCBV and qCBF maps were calculated and co-registered using Statistical Parametric Mapping version 12 (SPM12). Co-registration took place after quantification to prevent interpolation before deconvolution. First and second injection quantitative values were then compared voxel-by-voxel utilizing a linear model to determine the slope, intercept, r^2 and *p*-value.

Validation of Quantitative MR-Perfusion: Canine Data

Following successful demonstration of quantitative perfusion values for both first and second injections, a canine experiment was performed to compare MR-qCBF and MR-qCVR values against microspheres. Animal care guidelines of the University of Chicago were followed. Five mongrel dogs (20-30 kg) were studied at baseline and under physiologic stress (vasodilation) induced by CO_2 respiration. On the second day of the study animals underwent permanent endovascular occlusion of the M1 segment of the Middle Cerebral Artery (MCA). Here we present the results in of the physiologic challenge and imaging validation studies. Briefly, following induction, animals were anesthetized (1.5-2.0% isoflurane) and ventilated. Cardiac rhythm, end-tidal CO_2 (ETCO2), glucose, body temperature, hematocrit and arterial pressure were maintained within physiologic range. Imaging studies were performed immediately before and during physiologic stress. This study was designed to validate MRI-based physiologic perfusion imaging against reference standard neutron capture microsphere tissue perfusion.

MRI Scan Protocol

All MRI images were acquired on a 3 Tesla human magnet (Achieva, Philips Healthcare, Best, Netherlands). Animals were placed in the head first, prone position within a 15 channel receive-only head coil. Diffusion Weighted MRI (DWI) (field of view (FOV)=140x140mm, matrix = 128x128, number of excitations (NEX)=1, repetition time(TR)/echo time (TE) 192-2131/71, B-values= 0,1000 s/mm^2, Slice thickness (ST)=3 mm) was acquired on day 1 to rule out recent infarct, on day 2 DWI was acquired at 1, 1.5, 2, 3, and 4 hours post MCAO. Images of cerebral perfusion where quantified using a previously reported calibration technique which used pre-and

post-contrast T_1 maps to calculate parenchymal T_1 changes [47-49]. This approach acquires a 2D inversion recovery (FOV/Matrix =220/88, Slice Thickness= 6 mm, a single 2D slice) with variable delay time and the Look-Locker equation and EPI readout (LL-EPI) to quantify T_1 values within the image. The LL-EPI is coregisgtered with a DSC perfusion scan (FOV/matrix= 220 mm/88, single-shot, EPI, Fat Saturation, Nslices=5, Thickness= 6, TR/TE=25/335, 200 time points), taken concurrently with an injection (3 ml @ 2 ml/sec Gd followed by 20 cc @ 2cc/sec Saline Flush) of a gadolinium-based contrast agent (Multihance, Bracco, Princeton, NJ).

Microsphere Injection Protocol:

Microsphere injections were performed by hand with the animal stationary in the magnet. Each injection consisted of a 4 ml injection of 10^7 of neutron captured microspheres injected into the left ventricle of the heart over a period of 10 seconds by a neurointerventional radiologist (Dr. Gregory Christoforidis, MD, PhD). Reference blood draws were collected from a catheter placed in the abdominal aorta which was connected to a MRI compatible Harvard pump (PHD 2000, Instech, Plymouth Meeting, PA) set to withdraw with calibrated syringes (Monoject 20mL, Medtronic, Minneapolis, MN). Blood draws of 10 ml/min for 2:00 min yielded 20 ml of blood for analysis. Each blood withdraw was initiated 10 seconds prior to the microsphere injections which began once a flow of blood was observed into the withdraw tubes. Microspheres containing Gold, Samerium, Lutecium and Lanthium were used for baseline, hypercapnia, post-occlusion I and post Occlusion II, respectively. In addition to the brain, both kidneys were excised and analyzed to serve as an internal reference for normative perfusion. Upon completion of the microsphere injection, a contrast enhanced quantitative MR-perfusion scan was collected.

Carbon Dioxide Challenge Protocol:

Transient hypoxia was induced through respiration of carbogen gas (5% CO_2/95% O_2). End Tidal CO_2 ($ETCO_2$) was available throughout the experiment. To undergo hemodynamic challenge, animals breathed carbogen until a target $ETCO_2$ of 60 mmHg was achieved. When the targeted levels were reached, an arterial blood sampling of CO_2 was acquired from the Abdominal Aorta and microspheres were infused. Arterial blood gas was calculated with a point-of-care unit (Epoc, Alere, Overland Park, KS) within 1 minute of withdrawl. A post-hoc analysis revealed a calibration error between the InVivo monitoring of $ETCO_2$ and the reference value arterial CO_2 ascertained from the abdominal aorta, which resulted CO_2 elevation (Figure **5.1**). All analyses are done using calibrated CO_2 values.

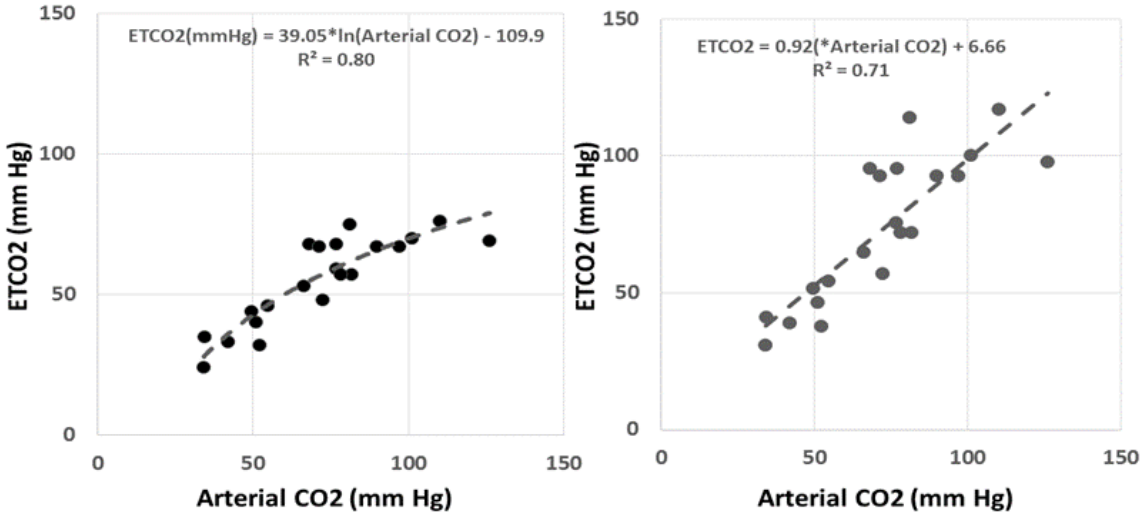

Figure 5.1: ETCO2 was Calibrated to Arterial Blood Sampling. End Tidal CO2 of respiration was calibrated to invasive sampling of blood directly from the abdominal Aorta. Since targeted hypercapnia of 60 mmHg was determined by ETCO2, physiologic hypercapnia was considerable higher than the targeted values of 60 mmHg

Microsphere Analysis

Upon completion of these imaging experiments the animal was returned to the vivarium and allowed to recover will full access to food and water. On Day 2 a terminal experiment to study ischemia in a permanent occlusion of the middle cerebral artery was performed. Upon completion of Day 2, animals were sacrificed for post-mortem analysis. After the animals were sacrificed, brains were surgically excised, sectioned, photographed, weighed and allowed to dry prior to microsphere counting. Brains were section into three coronal slices (Anterior, Middle,

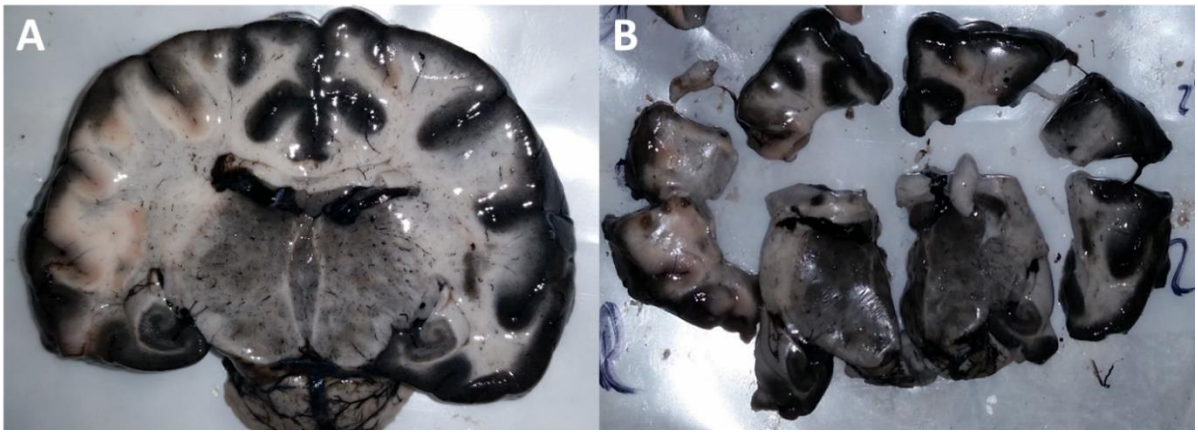

Figure 5.2: Example of sectioned animal brain. Shows a sample brain (A) slice and (B) sectioned into 9 sub-regions (inferior, middle, superior, right and three regions going center out and basal regions

Posterior) and each slice sectioned into 9 sub-regions (inferior, middle, superior, right and three regions going center out and basal regions, Figure **5.2**.

Microsphere counting was performed by BIOPAL (BioPhysics Assay Laboratory, Inc). A report of perfusion for each tissue sample, its reported weight (in g) as well as raw microsphere counts were reported. The general principle underlying neutron activation is that an incident neutron is captured by an atomic nucleus forming a radioactive nucleus. An ideal radioactive nucleus would be short-lived and emit a gamma-ray during the decay process (52). The energy

of the gamma-ray is discrete and distinct for each stable atom. High-resolution detection equipment is used to identify and measure the emitted gamma-ray. The number of emitted gamma rays is directly proportional to the total mass of the parent isotope allowing for proportional counting of the deposited spheres. Spheres counted in the calibrated (i.e. known blood withdraw rate) blood sample gives a reference for quantitative normalization of counts to perfusion.

MRI and Microsphere Registration:

A graphical user interface was developed to allow for registration of microsphere laden tissue samples to the MRI perfusion images, Figure **5.3**. A stainless steel holder designed for the sectioning of canine brains was used to create coronal sections with thicknesses equal to that of the 2D MRI slices used to measure perfusion. The user interface allowed for slice-by-slice comparison of MRI and photographs of the brain sections. Regions of interest were manually drawn and validated by an interventional neuroradiologist to ensure proper registration of microsphere samples and MRI images. The means and standard deviations for MR-qCBF within each ROI were calculated and compared to microsphere values.

Figure 5.3: Screenshot from Graphical User Interface. Screen shot from the graphical user interface developed to allow for registration of microsphere laden tissue samples to the MRI perfusion images.

Patient Data

A series of 16 consecutive patients with angiographically confirmed cerebral vascular disease who underwent an ACZ challenge MRI perfusion study as part of their standard of care were retrospectively selected. Cerebral perfusion was quantified using a previously reported DSC perfusion MRI pulse sequence (SCALE-PWI[47-49]). All patients were imaged in the clinic using a 1.5T (Avanto, Siemens) MR scanner with the following parameters: TR/TE = 1,090/34 msec, matrix size = 128 x 128, FOV = 220 mm x 220 mm, for an in-plane resolution of 1.72 mm, flip angle = 20°, Slice thickness = 5 mm, acceleration factor = 2, with 15 slices. A single dose injection (0.1 mmol/kg body weight) of Gd-DTPA (Magnevist Berlex, Princeton, NJ) was followed by a 15 mL saline flush, at 4 mL/s.

After the first DSC-MRI acquisition, the patient was immediately injected with 1000 mg of ACZ. The second DSC-MRI scan was then performed approximately five minutes after the

completion of the first using the same parameters described above. qCVR maps were generated by comparing baseline qCBF with challenged qCBF as described in Equation 37. Regions of interest (ROIs) around compromised areas were then drawn and disease stage was determined by a neuroradiologist using the resulting qCBV, qCBF and qCVR images. Mean and standard deviation of qCVR values comparing impaired vs non-impaired ROIs were calculated and analyzed. Significance was considered to be $p < 0.05$.

Image Post-Processing

For each subject, the time series images were automatically reconstructed on the scanner. The images were then accordingly de-identified (for patient studies), and post processed using in-house software developed in MATLAB (Mathworks, Natick, Massachusetts), using a Dell XPS 8500 (16 GB of RAM, Intel i7-3770 CPU @ 3.4 GHz). Standard deconvolution analysis was used[53,54]. AIF, sagittal sinus, and white matter were automatically segmented as described in [47-49]. A water correction factor was fit for each scanner and injection number. Quantitative CBV and CBF values were calculated using Equations 33 through 36. Quantitative CVR was then calculated after coregistration of perfusion images. Coregistration for all human subjects was done using Statistical Parametric Mapping version 12 (SPM12). Co-registration took place after quantification to prevent interpolation before deconvolution. No coregistration was done for canines. CVR was computed as a percentage difference between pre and post ACZ qCBF values Equation 37.

5.4 Results

Validation of Quantification in Multiple Injections: Volunteer Data

Volunteer data shows strong correlation between quantitative perfusion measurements between first and second injections. Figure **5.4** shows WCF curves fit to empirical data (blue represents first injection data, red shows second injection). For volunteer data (all 1.5T Espree data), $A_1 = 0.07175$, $B_1 = 0.0335$, $C_1 = 0.1$, $A_2 = 0.17076$, $B_2 = 0.0001$, $C_2 = 0.00$, where subscripts represent injection number. Table 3 shows slope, intercept, correlation, and p-values for qCBF-1st injection vs qCBF-2nd injection for each patient. Notice that the majority of slopes are close to unity and all correlations are higher than 0.90 ($r^2 > 0.90$). Table 4 shows the same data for qCBV-1st vs qCBV-2nd for each patient. Figure **5.5** shows combined data for (A) qCBF and (B) qCBV. Each blue point represents a single voxel value, with the x-axis representing 1st injection values, and the y-axis showing 2nd injection data. Notice both show high correlation ($r^2 > 0.92$) and near unity slopes for both qCBF and qCBV.

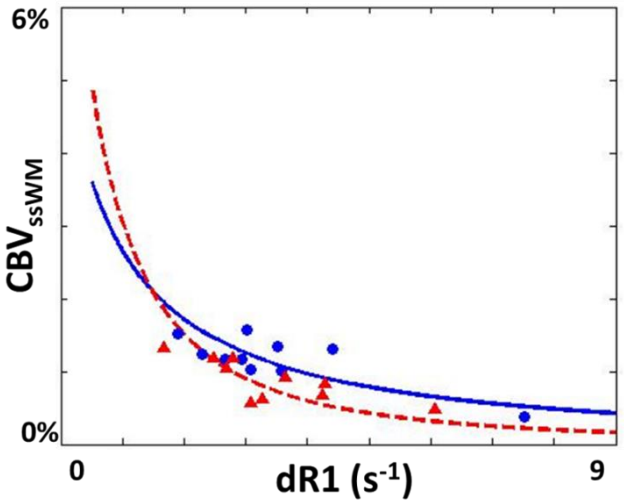

Figure 5.4: WCF curves fit to empirical data. Here blue represents first injection data and red shows second injection. Each dot represents data from one volunteer.

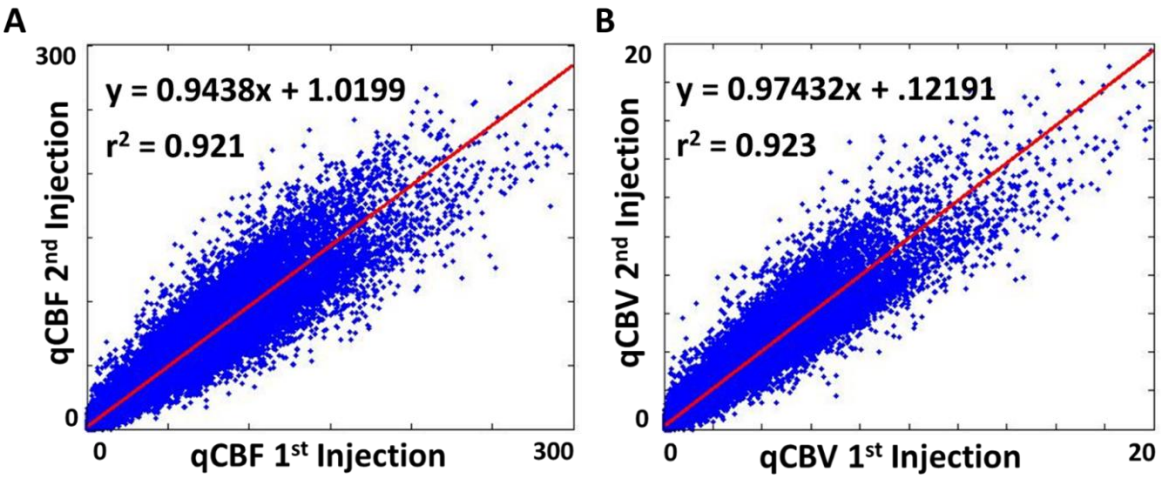

Figure 5.5: First and Second Injection Show High Correlation. Shows combined data for (A) qCBF and (B) qCBV. Each blue point represents a single voxel value, with the x-axis representing 1st injection values, and the y-axis showing 2nd injection data.

Table 3: Correlation between qCBF-1st injection vs qCBF-2nd injection for each patient

Volunteer	Slope	Intercept	R^2	P-value
1	0.74248	0.66305	0.973	p << .001
2	1.1294	0.20003	0.979	p << .001
3	1.2226	0.92919	0.985	p << .001
4	0.96323	0.33267	0.965	p << .001
5	0.66418	0.59089	0.973	p << .001
6	0.92642	2.2684	0.951	p << .001
7	0.99134	2.1161	0.902	p << .001
8	0.81619	1.2417	0.977	p << .001
9	0.94992	2.7679	0.919	p << .001
	0.94381	1.0199	0.921	p << .001

Table 4: Correlation between qCBV-1st injection vs qCBV-2nd injection for each patient

Volunteer	Slope	Intercept	R^2	P-value
1	0.89477	0.046481	0.964	p << .001
2	1.2373	0.033655	0.966	p << .001
3	1.3107	0.037853	0.994	p << .001
4	1.073	0.048448	0.951	p << .001
5	0.79986	0.049189	0.976	p << .001
6	1.1016	0.059403	0.966	p << .001
7	1.1235	0.071937	0.922	p << .001
8	0.81783	0.063081	0.979	p << .001
9	1.0072	0.209471	0.921	p << .001
	0.97432	0.12191	0.923	p << .001

Validation of Quantitative MR-Perfusion: Canine Data

Figure **5.6** shows representative qCBF and qCVR maps for the animal study. Baseline imaging was performed at CO_2 = 32 mmHg, while challenge was imaged at CO_2 = 64 mmHg. Notice that there is a substantial increase in qCBF in the cortical regions of the brain—resulting in qCVR reaching 200% in some regions. Figure 5.7 shows high correlation between MR-qCVR and microsphere qCVR (slope = 0.9684, intercept = 38.1833, r^2 = 0.66). Each blue dot represents 1 region while the red line shows the linear model fit. Furthermore, MR-qCBF showed high correlation with microsphere numbers (slope = 0.93511, intercept = 15.28, r^2 = .4547).

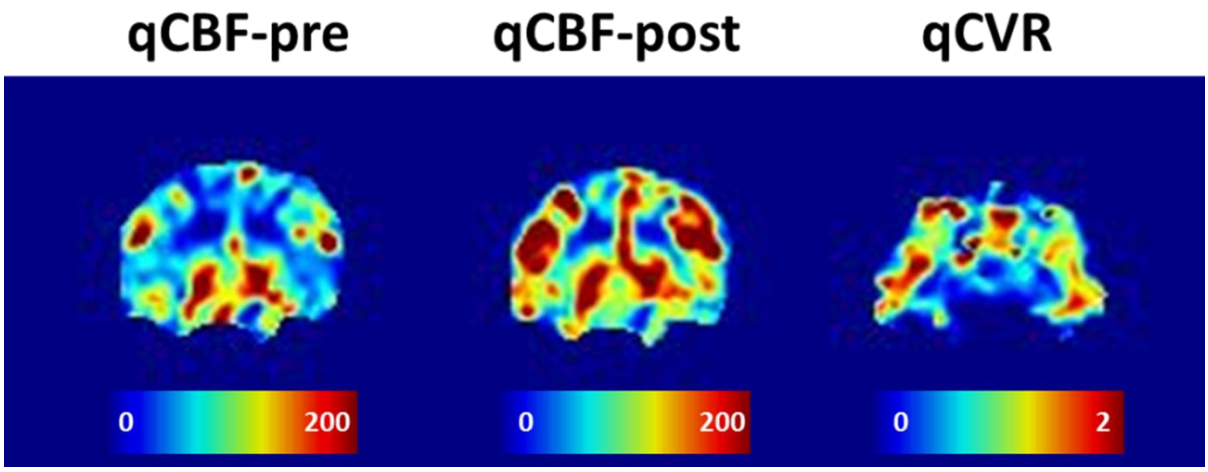

Figure 5.6: representative qCBF and qCVR maps for the animal study. Baseline imaging was performed at CO_2 = 32 mmHg, while challenge was imaged at CO_2 = 64 mmHg.

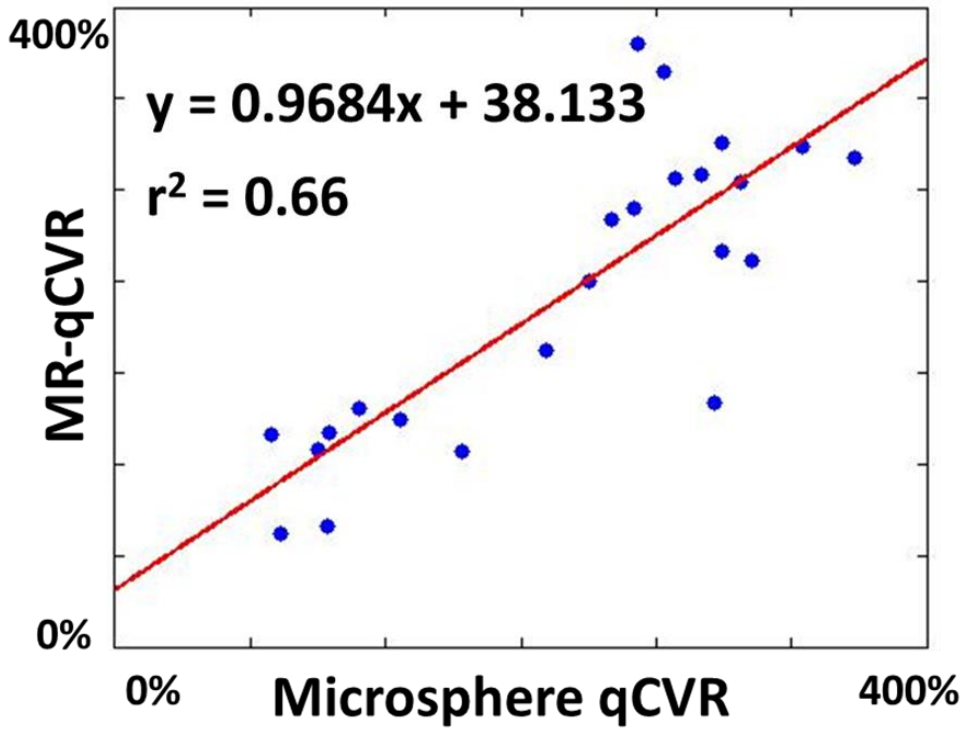

Figure 5.7: Linear regression shows high correlation between MR-qCVR and microsphere qCVR.

Patient Data

For all patient data (1.5T Avanto data) the WCF was empirically fit with coefficients, $A_1 = 0.02175$, $B_1 = 0.2125$, $C_1 = 0.1$, $A_2 = 0.02176$, $B_2 = 0.5935$, $C_2 = 0.01$, where subscripts represent injection number. Patient data show strong distinction between disease stage Figure **5.8**. In Figure **5.8**, the rows represent different patients with varying hemodynamic failure. The columns show pre and post ACZ qCBF maps an qCVR from left to right. Figure 5.9 shows a comparison between qCVR from non-impaired regions and impaired regions, the p-value was generated with a paired t-test. qCVR is significantly reduced in the impaired region compared to the healthy region (-13.1957 ± 7.8411 vs 9.4943 ± 7.744, $p < 0.0015$).

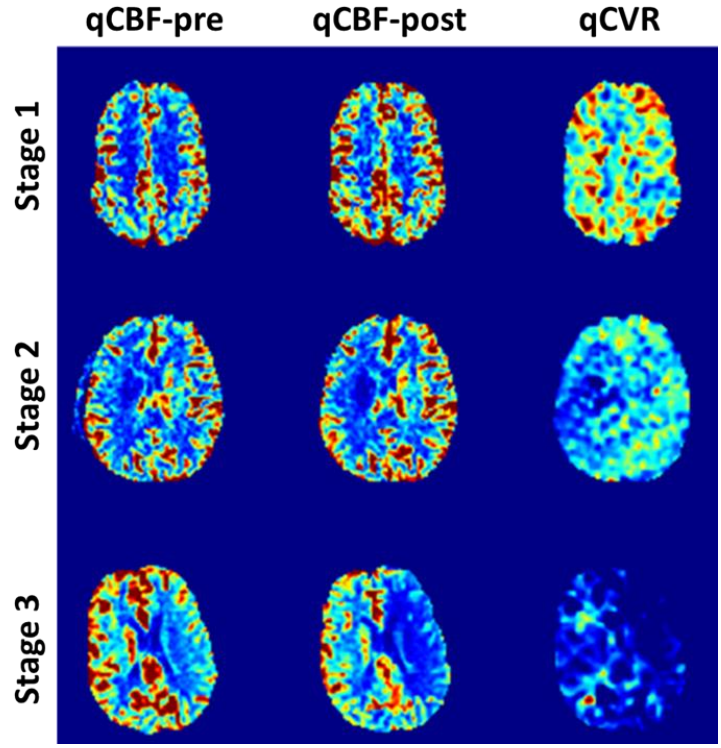

Figure 5.8: Representative qCBF and qCVR maps for the patient study. Patients chosen to show a range of hemodynamic compromise. The rows represent disease stage. The columns show pre and post ACZ qCBF maps an qCVR from left to right.

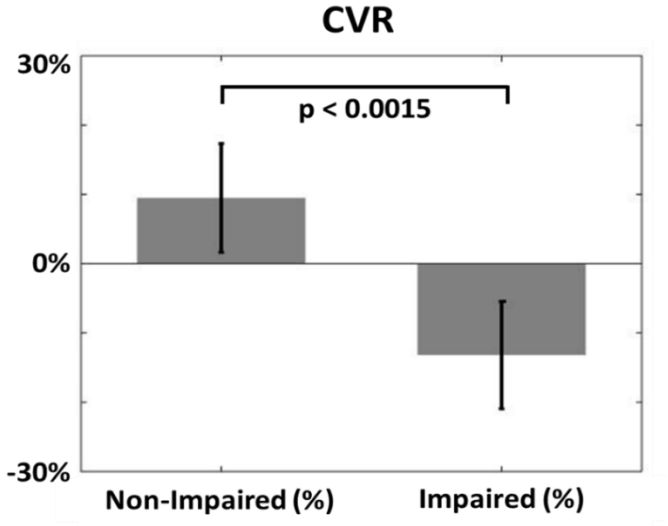

Figure 5.9: Comparison between qCVR shows significant reduction in impaired regions.

5.5 Discussion

In this study we found that serial quantitative DSC-MRI measurements allowed for accurate MR-qCVR calculations when compared to the microsphere reference standard. Volunteer data showed that measurements made from first and second injections were highly correlated (qCBF: slope = 0.94381, intercept = 2.7679, r^2 = 0.921; qCBV: slope = 097432, intercept = 0.12191, r^2 = 0.923). While one volunteer showed an outlying slope (slope = 0.66418 for volunteer 5), the others were within 20% of unity. Further examination shows the failure of volunteer 5 was the result in aberrant CBV_{ssWM} as a result of aberrant values within the WM mask. Upon removal of these outlying voxels, the slope improved to 0.89244.

Previous work validated the Bookend approach by quantifying CBF against PET data in patients with cerebrovascular disease (55). In this study, we show that correcting the second injection (with a WCF_{2nd} and CBV dilation correction), allows for serial quantitation of both CBF and CBV. By applying this to an animal model, we showed data displayed high correlation between qCBF numbers and excellent linearity correlation between MR-qCVR and qCVR measured via microspheres. Furthermore, absolute qCBF (measured by both microspheres and MR) during both baseline and challenge matched well with previously reported data (56). Taken in concert this validates the serial Bookend MR approach for qCVR proposed in this study.

Lastly, we retrospectively applied this method to 16 consecutive patients with angiographically confirmed cerebral vascular disease who underwent an ACZ challenge MRI perfusion study as part of their standard of care. We found qCVR in non-impaired tissue to be 9.49 ± 7.7%, slightly lower than previously reported CVR from ACZ challenge, which is

approximately 20 – 30%(57,58). This slight discrepancy is probably due to the fact that all our patients had some level of vascular impairment.

Recent work by Kawano et. al, has shown a negative correlation between MTT and CVR (59) in patients with Moyamoya disease. This is an interesting avenue for future study. All measurement techniques of CVR require some form of challenge (usually either ACZ or CO_2 inhalation). These challenges are not without risk, and thus any surrogate measurement would be clinically beneficial. Quantitative CVR may improve such analysis, and the correlation between MTT and CVR is a currently being researched within our group.

5.6 Conclusions

We present the first evidence of a method to accurately quantitate CVR using current MRI-protocols. We show that the use of a WCF specific to the second injection allows for accurate quantification of CBF and validate this in a canine model. Finally, we show that qCVR can clearly distinguish between stages of hemodynamic compromise.

Chapter 6 Ktrans Diffusion

6.1 Overview

Studies suggest that between 2-6% of the general population harbors an intracranial aneurysm (IA). While the vast majority of IAs remain dormant, approximately 30,000 rupture annually (5) causing devastating intracranial subarachnoid hemorrhage complications. Because of the inherent treatment risks associated with microsurgical clipping or endovascular coil embolization and the fact that only a small fraction of IAs rupture annually (<2%), treatment of unruptured IAs remains controversial (6,7). Consequently, a methodology to differentiate IAs with high rupture risk is greatly needed in the clinical environment.

Currently, the rupture risk and thus surgical intervention is determined by either patient specific (age, hypertension, smoking, alcohol/drug abuse, past or family history of aneurysmal subarachnoid hemorrhage) and/or aneurysm specific risk factors primarily related to anatomy such as size, location, or morphology (e.g. irregular contour (60) and daughter sacs (61)) as determined by CTA, MRA, or DSA imaging. Recently, however, several investigators have postulated new risk stratification paradigms, in which IA risk may be affected by local gene expression in the vascular wall such as the production of matrix metalloproteinases (MMP-2, MMP-9), ultimately thinning and remodeling the aneurysm wall to increase the rupture risk (62). This line of inquiry requires more direct evaluation of the wall with novel imaging biomarkers of wall instability and inflammation (62-68). In a recent study, it was hypothesized that thinner IA walls showed higher DCE-MRI wall permeability (i.e. k^{trans} and v_l) and were predictive of aneurysm wall stability (63). However, K^{trans} and v_l were derived from the standard Tofts-Kety permeability model (69) that assumes microscopic tracer permeability through capillaries and

into a tissue bed. The original Tofts model does not address contrast-extravasation through the aneurysm wall, which may better represent a macroscopic manifestation of microscopic capillary permeability. In particular, pharmacokinetic parameters provided by the Tofts model may reflect both contrast uptake into an inflamed aneurysm wall and the passive diffusion of contrast through a pathologically thinned wall into the cerebral spinal fluid (CSF). Without the spatial resolution required to directly image the IA wall typically measuring 20-100 microns, an alternative approach to modeling the signal changes associated with pharmacokinetics of the aneurysm wall is required.

6.2 Introduction

The leakage of gadolinium based contrast agents has long been used as a clinical tool that reflects pathophysiology in cancers. The Standard Tofts model (69,70) applied to Dynamic Contrast Enhanced (DCE) MRI describes the transport of contrast from the intravascular to extravascular space that is reflective of microstructural tissue changes. In particular, Tofts modelling has been shown to reflect angiogenesis (71-75). Clinical translation of the Tofts model has been wildly successful and yields actionable information in tumor aggressiveness and response to anti-angiogenic chemotherapies (74,76,77). However, kinetic modelling of DCE images can yield anomalously high values of the factional volume of extravascular extracellular space (v_e) and contrast agent permeability rate (k^{trans})in some cases (78). This has prompted study by several researchers to improve upon the standard Tofts Model. For example, incorporating intravascular signal (69) and diffusional transport of contrast agent (78,79) have been developed and show significantly altered calculated parameters.

Unfortunately, the computational complexity of diffusion correcting k^{trans} is costly. Some direct models take between 1 minute and up to several hours per pixel of computing time (78). One goal of this work is to compare the accuracy of optimized, long chain diffusion correction with a parameterization of diffusion leakage derived from simulations. The development of an easily implementable approximation to the Pellegrin model (79) has the potential to allow more widespread use of the proposed improvements on the Tofts model. Furthermore, prior studies of diffusional correction to k^{trans} were performed in tumors (78), where leakage and diffusion occur within the same voxel creating the potential for mixed-effects in the modelling.

In this study, we evaluate the diffusional transport term in the modified Tofts model in a unique application, that of intracranial aneurysm (IA). The Standard Tofts model has been shown to be clinically significant a predictor of rupture risk in intracranial aneurysms and is currently being evaluated as a metrics where by k^{trans} reflects the thickness of an aneurysm wall (63). For the purpose of understanding diffusional transport corrections to the Tofts model, brain aneurysms represent an ideal physiologic milieu: the aneurysm wall serves as a single distinct source of contrast through surface extravasation at the aneurysm dome, the leakage occurs directly into tissue which is characterized by low background leakage due to the presence of an intact blood brain barrier, and local diffusion of the brain parenchyma is well understood through extensive study of Apparent Diffusion Coefficient (ADC). These three factors allow us to separate diffusion transport from nominal k^{trans} "leakage" and to study these two effects separately *in vivo*.

Previous work by Fluckiger (78) and Pellerin (79) demonstrated that estimating kinetic parameters in the presence of passive contrast diffusion improved physiologic representation and

reduced the likelihood of returning unphysical v_e values, especially in poorly perfused regions. We apply a diffusion compensated Tofts model (DC-Tofts) to analyze contrast kinetics at the surface of an IA wall. By incorporating the effects of passive diffusion within the parenchyma, the DC-Tofts model may more accurately represent contrast kinetics at the surface of an IA wall, and the macroscopic phenomena of contrast agent leakage into or through it. The purpose of this study was to quantify diffusion compensated IA wall permeability (k^{trans}, v_e), and to develop a rapid method to determine diffusional effects using parameterization based on easily accessible ADC values.

6.3 Methods

We performed a mathematical simulation of our diffusion compensated Tofts model in the setting of an IA which we model as a local source of contrast. Next, we compared diffusion-corrected to uncorrected values in a study of human IAs. We then propose a parameterization of the diffusion corrected rate constant (k^{trans}_{DC}) as a function of tissue specific diffusion rate (D), k^{trans} and fractional plasma volume (v_p). Finally, we perform a re-analysis of an existing dataset (first reported in (63)) to determine if diffusion corrected kinetic parameters improve the risk identification of aneurysms. This investigation was HIPAA (Health Insurance Portability and Accountability Act) compliant and was approved by the local IRB (Institutional Review Board) at our institution. All subjects provided written informed consent.

Theory

Permeability Modeling

The Tofts Model is well known and used frequently in a variety of research and clinical settings. It describes the vascular delivery and distribution of a tracer into the extracellular

volume and has been used with great success to quantify the leakage of gadolinium-based contrast agents in solid tumors with notoriously leaky vasculature (neovascularity). Since an intact blood brain barrier (within healthy brain tissue) restricts the distribution of contrast, the Tofts model can be used to quantify the leakage rate through a compromised blood brain barrier (72,73,76,80). While pathological tissue enhancement is adequately explained by leakage of tumor neovasculature, the presence of contrast enhancement in necrotic centers which lack a blood supply is less understood.

A similar problem arises when considering the Tofts model to explain contrast uptake into and across the aneurysm wall. In IA patients, their vasculature (barring the aneurysm) is largely unaffected—suggesting the blood brain barrier is intact and thus contrast enhancement should be minimal. However, as was previously shown (63), contrast can be readily observed beyond the compromised and thinned IA walls. Consequently, we have applied the DC-Tofts model to account for contrast extravasation through the vascular lumen and aneurysm wall into the CSF as well as diffusion from higher concentrated regions towards lower concentrations.

The permeability-limited Modified Tofts Model (69) quantifies the kinetics of a tracer leaking through a semi-permeable membrane with the following relationship:

$$\mathbf{C(t)} = \boldsymbol{k^{trans}} \int_{\mathbf{0}}^{\boldsymbol{t}} \boldsymbol{e^{-k_{ep}(t-\tau)} C_p(\tau) d\tau + v_p C_p(t)} \qquad (38)$$

with k^{trans} dictating the tracer transfer rate from the intravascular into the extracellular extravascular space with units of min^{-1}, $k_{ep} = k^{trans}/v_e$ in units (min^{-1}) describing the ratio of the transfer rate (k^{trans}) to the fractional volume of tracer (v_e), $C_p(t)$ the intravascular tracer

concentration, that is, the Arterial Input Function (*AIF*), *C(t)* is the voxel tracer concentration and v_p the fractional plasma volume.

The diffusion-corrected model improves on the Tofts model by including a diffusion term when calculating the changes in concentration as a function of time—modeled by Equation 39 (78,79)

$$\frac{dC_D(t)}{dt} = k^{trans}C_p(t) - k^{trans}\frac{C_i(t)}{v_e i} + \sum_N \frac{\left(\frac{D_i + D_N}{2}\right)}{a^2}\left(\frac{C_N(t)}{v_{eN}} - \frac{C_i(t)}{v_{ei}}\right) \qquad (39)$$

where *a* is the in plane voxel length, C_D is the diffusion compensated tracer concentration, *D* is the voxel specific diffusion constant, and *C* is the measured concentration. The subscript *i* refers to the voxel of interest while *N* refers to the adjacent neighbors (a total of 4 neighbors are included along the 2D plane).

Since IAs are surrounded by the pial surface of the cerebral cortex, remote from white matter with its well-known and complex diffusion function, we are able to reduce the computational complexity of the solution by approximating the diffusion rate (*D*) to be uniform in the extravascular space and replace $(D_i + D_N)/2$ in Equation 2 with a single parameter, *D*. We are then left with Equation 40.

$$\frac{dC_D(t)}{dt} = k^{trans}C_p(t) - k^{trans}\frac{C_i(t)}{v_e i} + \sum_N \frac{D}{a^2}\left(\frac{C_N(t)}{v_{eN}} - \frac{C_i(t)}{v_{ei}}\right) \qquad (40)$$

To solve for the concentration time-courses in each voxel we integrate and include the plasma concentration term, Equation 41. Note that this is the same as Equation 1, but we have added a new "diffusion term" defined as the 3rd term (**Bolded**) in:

$$\boldsymbol{C_{DC}(\mathrm{t}) = k^{trans} \int_0^t e^{-k_{ep}(t-\tau)} C_p(\tau) d\tau + v_p C_p(t) + \int_0^t \sum_N \frac{D}{a^2} \left(\frac{C_N(\tau)}{v_{eN}} - \frac{C_i(\tau)}{v_{ei}} \right) d\tau} \quad (41)$$

Simulation

To examine the effects of partial volume averaging and contrast diffusivity on contrast kinetics, we performed a 2D computer simulation. A single slice was used for simulations because the slice thickness in the DCE-MRI patient experiments was four times greater than in-plane resolution. Consequently, we estimated the inter-plane diffusion of contrast to be negligible compared to in-plane diffusion.

The simulated aneurysm model consisted of 3 different compartments—intravascular blood, vessel wall, and interstitial tissue (Figure **6.1**a-b). The concentration of contrast in the blood was modeled with a population-averaged *AIF* derived from clinically collected aneurysm patient information (shown in Figure **6.1**d). Simulated vessel wall and tissue compartment permeabilities (k^{trans}_{true}, v_{etrue}, v_{ptrue}), distribution volumes, and diffusion rates (D_{true}) were allowed to vary within known physiologically realistic ranges (63,78) (Table 5). With the known kinetic parameters and the population averaged *AIF*, we generated a 512x512 parametric image of contrast concentration which was allowed to evolve over time, *C(x,y,t)*. The concentration time courses were convolved with a 2D Gaussian kernel (full width half maximum (FWHM) = 2.73 mm) and resampled onto 64 x 64 matrix to match the in-plane experimental imaging resolution 0.58 mm x 0.58 mm, where the vessel wall width was estimated to be 50-550 microns

(81-83). Next we converted concentration curves into signal intensities (84) then added Rician noise to the signal time courses to create a uniform signal-to-noise ratio of SNR ~ 6.0. Finally, signal curves were converted back to concentration time course which were then fit to determine k^{trans}, v_e, and v_p values for both the Tofts model and the DC-Tofts model (examples shown in Figure 1e).

To examine how inputs parameters affected each model, k^{trans} and $k^{trans}{}_{DC}$ were studied at varying distances from the vessel wall. Model variations are also shown in histograms of k^{trans} - $k^{trans}{}_{DC}$.

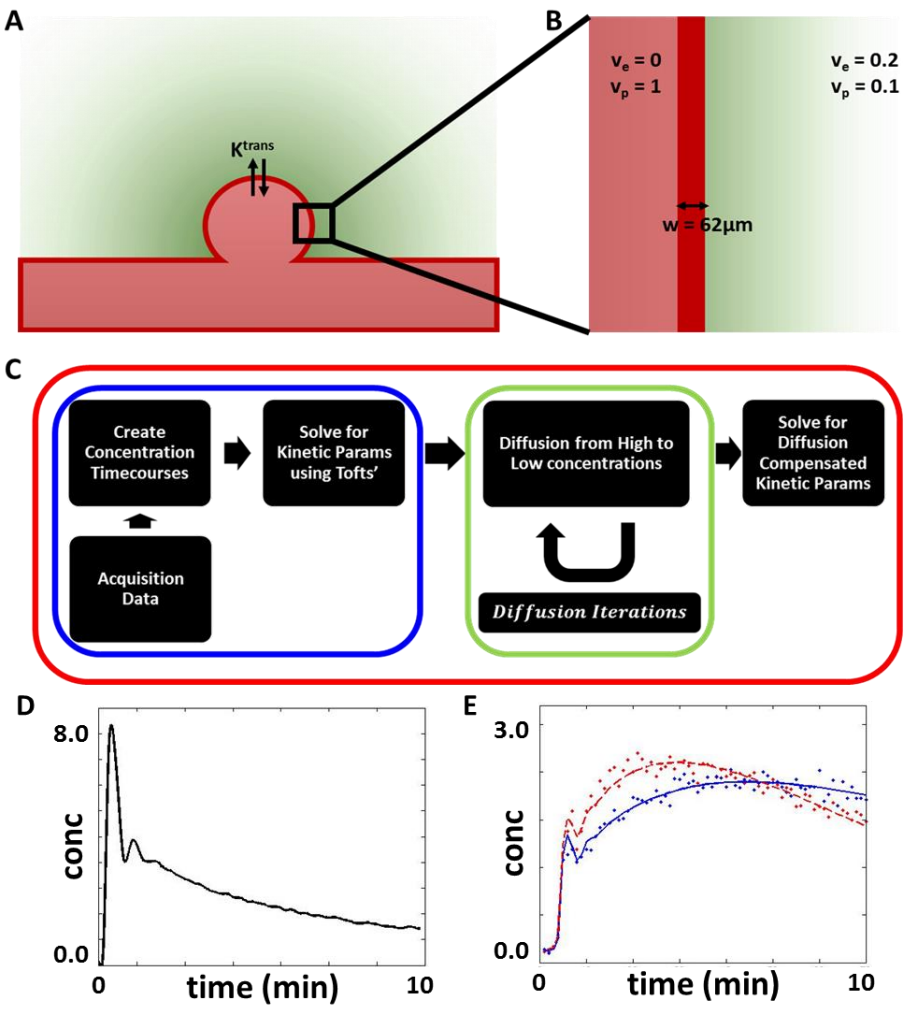

Figure 6.1: Simulation Schematic. (A) Schematic of leakage out of aneurysm and diffusion out toward area of low concentrations. Regions of darker green represent higher concentrations (B) Schematic of simulated environment. (C) Flow chart of diffusion compensated method. Blue outline represents the typical Toft's method. The Green outline highlights the diffusion compensation addition. Red outline is complete proposed method. (D) Patient averaged AIF used in simulations. (E) Simulated concentration curves for a single voxel. Dots represent noisy data, lines represent model fits. Blue represents standard Tofts model, while Red represents DC-Tofts.

Table 5: Simulation value Ranges

	Intravascular	Vessel Wall	Interstitial Tissue
K^{trans}_{true} (min^{-1})	0.0	0.8	0.02
v_{e_true} (%)	0.0	10	1.0 – 20
v_{p_true} (%)	1.0	0.0	5.0
D_{true} (10^{-3} mm^2/s)		5.0	0.01 - 10

Patient Data

All *in vivo* data in this study were collected prospectively between July 2011 and July 2013 on consecutive patients with unruptured IAs reporting for neurointerventional consultation at our institution. These collected data were initially published in (63). Major exclusion criteria included typical contraindications to MR imaging: pregnancy, contrast allergy, renal insufficiency, presence of MR incompatible implants, and prior IA treatment.

Imaging Protocol

Twenty-six cerebral aneurysms in 24 patients were imaged on a 3T (Trio, Siemens) MR scanner. To localize the IA for DCE imaging volume placement, a 3D time of flight (TOF) MRA sequence was acquired. DCE-MRI was performed using a single dose (0.1 mmol/kg) bolus injection of T_1-shortening contrast agent (Magnevist, Berlex; Wayne, NJ). The following image parameters were used: TR/TE=2.84 ms/0.8 ms, matrix= 128x128 - 384x384, FOV = 190-220 mm, and 12-24 partitions placed to adequately cover the IA, resulting in voxel dimensions between 0.58 x 0.58 x 2.0 mm and 1.48 x 1.48 x 5.0 mm. T_1 weighted images were acquired using a standard multi-phase 3D-gradient recalled echo (GRE) pulse sequence every 10 second for approximately 8 minutes. Partial Fourier was employed to increase temporal resolution to 5 seconds. Pre-contrast T_1 values ($T_{1,0}$) of the tissue, used to estimate contrast concentrations, were found by varying the flip angle (α= 5°, 10, 12, 15, 20, 25) and solving the spoiled gradient echo equation (63,85,86).

Post Processing

All permeability modeling and post-processing analyses were performed using in-house software developed in MATLAB (Mathworks, Natick, Massachusetts). Using a Dell XPS 8500

(16 GB of RAM, Intel i7-3770 CPU @ 3.4 GHz) computational time for contrast kinetic parameters was less than 10 minutes per slice.

Tofts Modeling

Kinetic modelling was performed in manually drawn large ROIs which contained the IA, a segment of the parent artery and the adjacent parenchyma. For every voxel within the ROI (including intra-vascular voxels) a Levenberg-Marquardt curve fit was utilized to find the k^{trans}, v_e, and v_p in Equation 1 that best fit the measured signal *C(t).*

Diffusion-Compensated Modeling

Direct voxel-by-voxel fitting of Equation 2 is heavily dependent on neighborhood values and thus any direct solution requires iterative fitting of diffusion coefficient, *D* and kinetic parameters, k^{trans}, v_e, and v_p for each voxel location. It has been previously shown that for even relatively small coverage, any direct solution becomes too computationally expensive (79). Consequently, we constrain the solution set to allow for faster implementation. First, as in previous work, *D* is not used as a free parameter (79). We instead assume a constant value for the diffusion rate ($D = 1.0 \times 10^{-3}$ mm^2/s for all model comparisons and risk analyses) across the whole brain. By assuming a constant diffusion rate, we can first solve for the diffusion term in Equation 4 and subsequently solve for the kinetic terms using a Levenberg-Marquardt algorithm with the diffusion term fixed at the value determined above. *D* was fixed at 1.0×10^{-3} mm^2/s to be slightly higher than white and grey matter values (0.7 and 0.9 respectively (87)). This was done because large vessels of the brain are surrounded by cerebral spinal fluid (CSF) which on a whole will increase the diffusion coefficient of the voxel. We examined the fidelity of this

assumption by re-calculating *in vivo* data varying D from 0.2 to 2.5 x 10^{-3} mm^2/s (discussed below).

Concentration maps at each time point are allowed to diffuse in increments of time. Because the image temporal resolution is roughly 5 secs, we use 5 "diffusion steps", enabling us to compute diffusion every Δt = 1 second (similar to (79)). During the diffusion calculations, v_e for each voxel was estimated as standard Tofts modelling, v_e. For each voxel and time point t we subtract the diffusion term from each side of Equation 4 and generate diffusion-compensated concentration curves. We then utilized the same Levenberg-Marquardt algorithm described above to solve for diffusion corrected kinetic parameters, $k^{trans}{}_{,DC}$, $v_{e\text{-}DC}$, and $v_{p\text{-}DC}$. A schematic of the work flow is shown in Figure **6.1**c.

Contrast Leakage through Aneurysm Wall

To investigate contrast leakage through the IA wall versus uptake and retention of contrast within the IA wall, we compared the probability density function (PDF) and cumulative density function (CDF) of ($k^{trans} - k^{trans}{}_{DC}$) between simulated and patient data. Simulated data were created over a wide range of D_{true} (Table 1). Best and worst fitting distributions were determined based on the Sum Square Error (SSE) between simulated and patient CDFs.

Model Comparisons

Several methods were used to compare the Toft's model with the diffusion compensated model using different regions of interests (ROIs). To remove any bias introduced by user-defined selection of kinetic parameters, kinetic parameters were automatically selected to include only voxels with corresponding v_p smaller than 0.8 ($v_p < 0.8$) were considered in evaluation.

This approach ensures that voxels with DCE signal of greater than 80% from partial volume averaging between the parenchymal signal and intravascular signal (i.e. inside the parent artery and/or IA) are removed.

For all direct voxel-by-voxel comparison of k^{trans} and v_e values, a large ROI was placed on a single slice containing the IA. The ROI was placed in a manner to fully encompass the aneurysm as well as all surrounding healthy vasculature. To examine how k^{trans} and v_e differed at the IA wall only, voxels within the large ROI with v_p values between 0.5 and 0.8 were used ($0.5 < v_p < 0.8$). Surrounding tissue was classified by v_p values between 0.01 and 0.5 ($0.01 < v_p < 0.8$). In each case, we utilized a linear model to determine the r^2 and p-value between the DCE-parameters (k^{trans}, v_e) of each model.

To investigate model differences as a function of distance from the aneurysm wall, we binned permeability parameters based on v_p. Again, high v_p was considered to be close to the aneurysm wall. The means and standard deviations of each bin were calculated and analyzed.

Mean k^{trans} and v_e values were also measured adjacent to the wall of a healthy parent artery in each patient and compared against mean k^{trans} and v_e values adjacent to the aneurysm wall. For both the healthy artery and the IA wall, ROIs were 5 voxels wide surrounding and outside the structure of interest. Average k^{trans} and v_e measurements from the aneurysm wall were compared with the parent artery values which served as internal controls (i.e. non-disease values) using a Student's unpaired *t*-test to determine if the DCE measurements were significantly different. Average permeability parameters were also compared on an inter-model basis using a Student's unpaired *t*-test. In all cases, statistical significance was defined at the 5% level.

DC Model Analysis and Parameterization

To dramatically reduce post-processing time, we utilized a homogeneous constant D = 1.0 x 10^{-3} mm^2/s. To examine the fidelity of this assumption, we re-analyzed *in vivo* data varying D from 0.2 to 2.5 x 10^{-3} mm^2/s. For each D, mean k^{trans}_{DC} and v_{eDC} values were calculated adjacent to the aneurysm wall ($0.5 < v_p < 0.8$). K^{trans}_{DC} and v_{eDC} were then fit as functions of diffusion constant, D, and k^{trans}.

We next investigated parameterizing k^{trans}_{DC} as a function of tissue specific D, k^{trans} and v_p. To do this we used the large ROI including both surrounding tissue and the aneurysm wall and fit Equation 3 for parameters a, b, c and d, by minimizing the sum square difference between the long chain k^{trans}_{DC} and the parameterized $\hat{k}^{trans}_{Corr}$.

$$\widehat{\boldsymbol{k}}^{\boldsymbol{trans}}_{\boldsymbol{Corr}} = \boldsymbol{k}^{\boldsymbol{trans}} + \boldsymbol{a}\left(\boldsymbol{v_p} - \boldsymbol{b}\right)^{\boldsymbol{2}} + \boldsymbol{c}\sqrt{\boldsymbol{D}} + \boldsymbol{d}\boldsymbol{v_p}\boldsymbol{D} \tag{42}$$

To analyze the predictive value of k^{trans}_{DC} parameterization, while preventing over-fitting, we performed a Leave One Out Cross Validation (LOOCV) study. In the LOOCV analysis, patient specific constants (a_i, b_i, c_i, and d_i) were fit using Equation 42.

$$[\boldsymbol{a_i}, \boldsymbol{b_i}, \boldsymbol{c_i}, \boldsymbol{d_i}] = \underset{[\boldsymbol{a},\boldsymbol{b},\boldsymbol{c},\boldsymbol{d}]}{\mathbf{argmin}} \sum_{\boldsymbol{n \neq i}} \left(\boldsymbol{k}^{\boldsymbol{trans}}_{\boldsymbol{DC}} - \widehat{\boldsymbol{k}}^{\boldsymbol{trans}}_{\boldsymbol{Corr}}\right)^{\boldsymbol{2}} \tag{43}$$

For example, because this study included 23 saccular aneurysms, patient specific constants (a_i, b_i, c_i, and d_i) were fit using data from the other 22 aneurysms. For each patient, we then calculated $\hat{k}^{trans}_{Corr}$ and compared it to the long-chain k^{trans}_{DC} with a linear model. Correlation and Bland Altman graphs for both surrounding tissue and the aneurysm wall were generated.

Clinical Consequence of Diffusion Compensation

To determine the clinical benefits of the DC-Tofts model, rupture risk was evaluated using mean values of DCE permeability parameters calculated in automatically drawn ROIs containing voxels adjacent to the aneurysm wall. ROIs were placed on a single slice containing the aneurysm where the highest k^{trans} values were observed. Aneurysm wall was defined as regions with v_p values between 0.5 and 0.8 ($0.5 < v_p < 0.8$). To examine only the regions of highest k^{trans}, the ROI was refined to only include the highest 25% of wall values.

Statistical Analysis and Risk Classification

Using previous published methodology (63), IAs were classified into high-risk and low-risk categories using two size-independent risk assessment paradigms. In clinical risk paradigm A, high-risk aneurysms were those that presented with neurological symptoms relevant to the aneurysm's location (headaches, mass effect, cranial neuropathy); asymptomatic aneurysms were low risk. In risk paradigm B, high-risk aneurysms harbored one of the following three imaging/anatomic properties: (1) multilobulated dome or blebs as defined by DSA or CTA, (2) presentation with multiple IAs, or (3) posterior circulation location; all others were defined as low-risk. Size indices were not used to define the risk profile for any aneurysm in Group A or B.

Univariate regression analyses were performed for groups A, B and AB (which was defined as A or B). High and low risk groups were compared against patient age, sex, aneurysm size, k^{trans}, and ($k^{trans} - k^{trans}_{DC}$). Multivariable logistic regression analysis was also performed to evaluate independent predictors of risk in the aforementioned risk paradigms/groups. In all risk analyses, only saccular aneurysms (n = 23) were examined. Significance was defined as <0.05 in all statistical tests.

6.4 Results

Simulations

Simulations (Figure **6.2**) were performed comparing Tofts model results versus diffusion compensated results with respect to environmental diffusion constant D_{true}, wall thickness, and v_{e_true}. Diffusion compensation tended to increase k^{trans} values close to the wall, while slightly reducing them further from the wall. Both close to the wall and in the surrounding tissue, $k^{trans}{}_{DC}$ was closer to true simulated $k^{trans}{}_{true}$ (represented by the black line). The bottom row shows probability distributions of ($k^{trans} - k^{trans}{}_{DC}$) in the 1000 simulations which clearly show that the diffusion constant D_{true} has a dramatic effect in ($k^{trans} - k^{trans}{}_{DC}$), while both width and v_e have little effect. A larger diffusion constant means that contrast will diffuse faster and further away from the wall. Without correcting for this effect the Tofts model will underestimate the amount of contrast near the source (aneurysm wall), and overestimate it in healthy tissue.

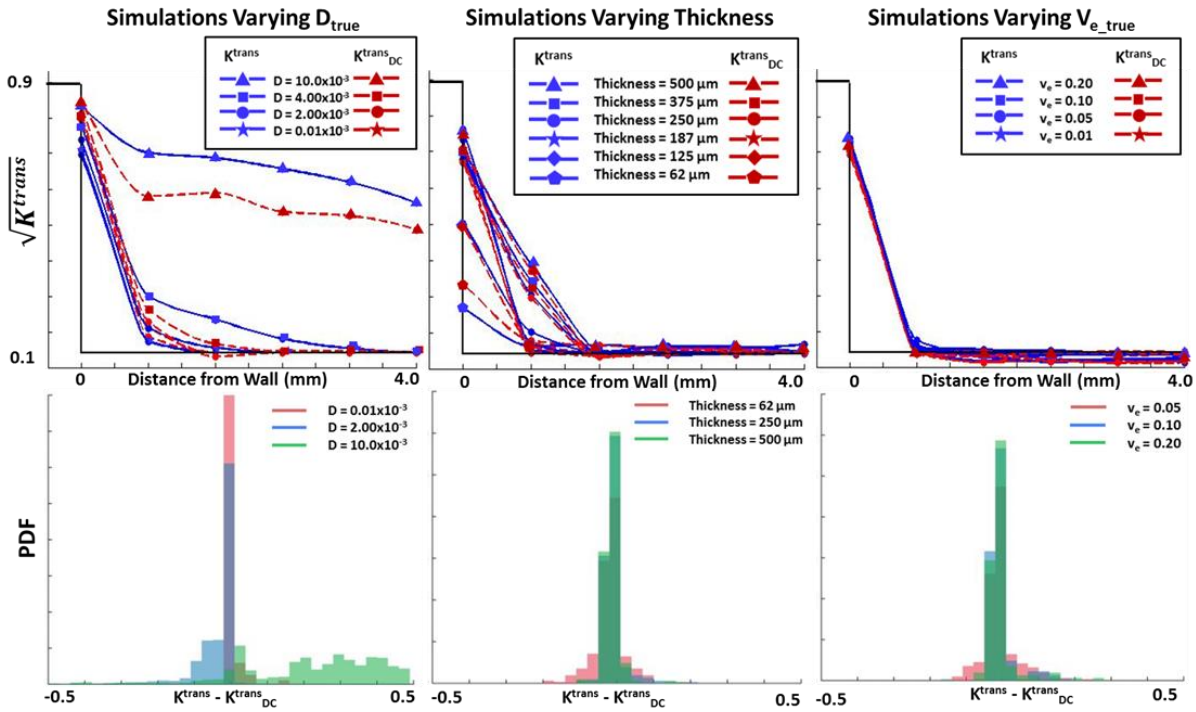

Figure 6.2: Simulated Results. Simulations show k^{trans} is predominately affected by diffusion constant D_{true} while minimally affected by v_{e_true} and wall thickness. The top row represents, k^{trans} values on the y-axis vs distance from vessel wall on the x-axis. The solid blue lines represent Tofts model results, while the dotted red lines are diffusion compensated results. The dots shown are mean k^{trans} from 1000 simulations. Black lines show k^{trans}_{true} values. Notice diffusion compensation tends to increase k^{trans} values close to the wall, while slightly reducing them further from the wall. In both cases moving k^{trans}_{DC} closer to true values. The bottom row shows the probability distributions in ($k^{trans} - k^{trans}_{DC}$) in the 1000 simulations. Note diffusion constant D_{true}, has a drastic effect in ($k^{trans} - k^{trans}_{DC}$) while wall thickness and v_{e_true} have little effect.

Contrast Leakage through Aneurysm Wall

Figure **6.3** shows probability (a,b) and cumulative (c,d) distribution functions of (k^{trans} – $k^{trans}{}_{DC}$) for measured data (represented in blue) and simulated data. Simulated data was done over a wide range of values for D_{true}. The best and worst fitting distributions are shown, red represents simulation results from D_{true} = 2.0 x 10^{-3} mm^2/s (Best fit with SSE = 0.128). Green represents simulation data from D_{true} = 0.01 x 10^{-3} mm^2/s (Worst fit with SSE = 1.440). Considering, previously published data show diffusion coefficients within the brain vary from approximately 0.6 to 2.7 x 10^{-3} mm^2/s (low end white matter to CSF) (87), these results taken in concert suggest contrast is actively leaking through the aneurysm wall and diffusing outward.

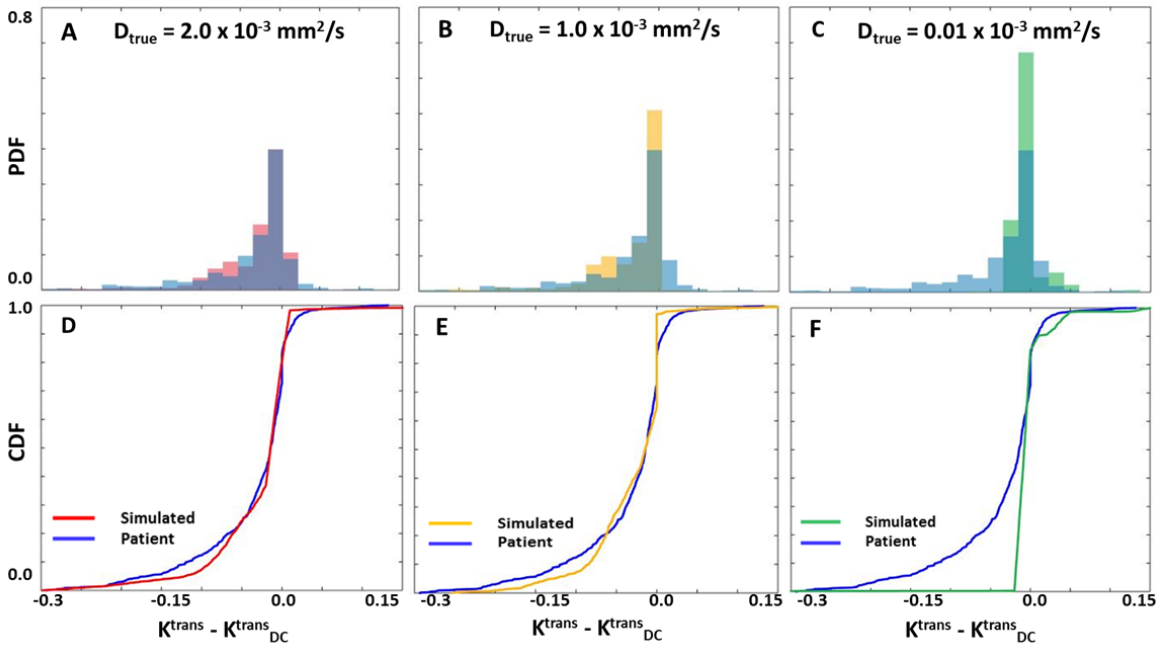

Figure 6.3: Simulated data suggests contrast leakage through the aneurysm wall. Probability (A,B) and cumulative (C,D) distribution functions of (k^{trans} – $k^{trans}{}_{DC}$) for measured data (represented in blue) and simulated data. Red represents simulation results from D_{true} = 2.0 x 10^{-3} mm^2/s. Green represents simulation data from D_{true} = 0.01 x 10^{-3} mm^2/s.

Model comparisons

Correlation between voxel-wise DCE parameters of both models are high. Measured k^{trans} and v_e values from both models are shown to be highly correlated. (k^{Trans}: $r^2 = 0.821$, slope = 1.02, intercept = 0.009, p < 0.0001; v_e: $r^2 = 0.723$, slope = 0.797, intercept = 0.014, $p < 0.0001$). Figure **6.4**a and d show correlation between models in surrounding tissue. (k^{Trans}: $r^2 = 0.851$, slope = 1.00, intercept = 0.008, p < 0.0001; v_e: $r^2 = 0.718$, slope = 0.827, intercept = 0.012, $p <$ 0.0001). Figure **6.4**b and e show measured k^{trans} and v_e values from both models adjacent to the aneurysm wall. We see a divergence at the wall between the models, but correlation remains high (k^{trans}: $r^2 = 0.761$, slope = 1.067, intercept = 0.0165, $p < 0.0001$; v_e: $r^2 = 0.717$ slope = 0.682, intercept = 0.013, $p < 0.0001$).

Figure **6.4**c and f, show model divergences as a function of distance from aneurysm wall. Error bars show standard deviation around mean binned values. Though noisy, k^{trans}-k^{trans}_{DC} clearly shows divergence near the wall fluctuating from -0.071 to 0.013 as v_p decreases from 0.8 to 0.01. Though more subdued, v_e-v_{eDC} also shows a clear trend decreasing from 0.011 to -0.002 as v_p decreases from 0.8 to 0.01.

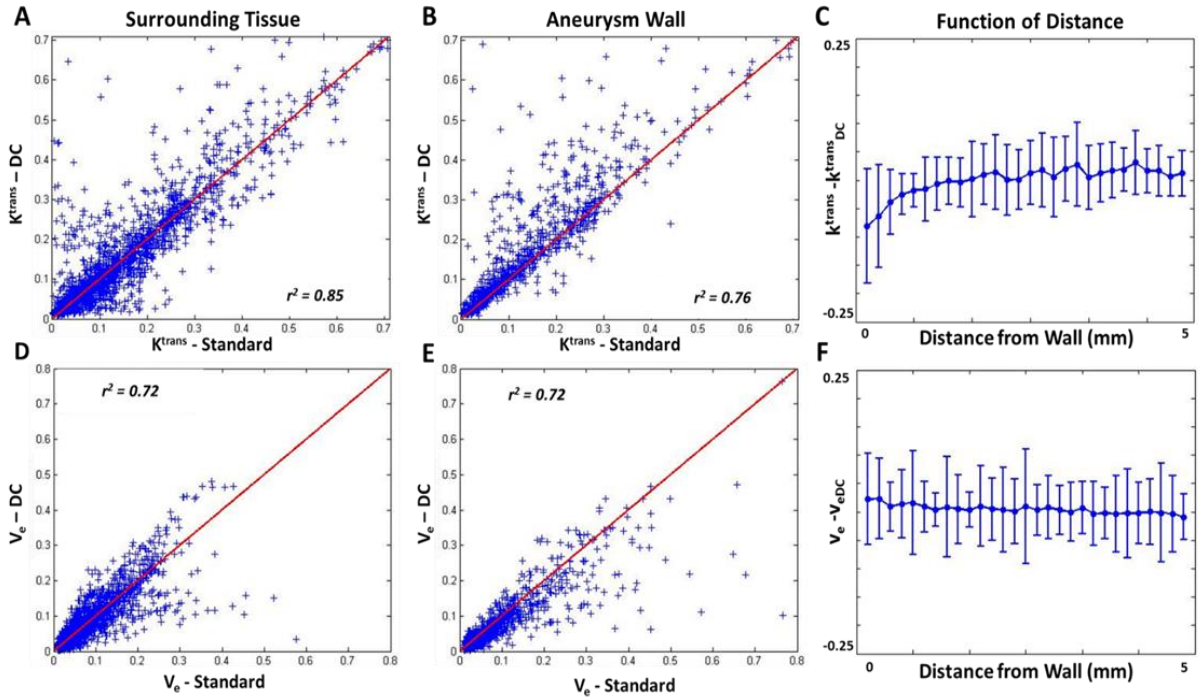

Figure 6.4: A comparison of Tofts and DC-Tofts models shows high correlation between the models. Divergence between methods tended to occur near aneurysm wall. All images show the line of unity for visual purposes. The reported correlation coefficients (r^2) are from a linear regression (line not shown.) (A and D) pixels from surrounding tissue. (D and E) show pixel comparisons near the aneurysm wall. (C and F) show model divergence as a function of distance from the wall.

Figure **6.5** shows a comparison between k^{trans} values in Tofts and DC-Tofts models from healthy vessels and aneurysm walls, p-values were generated with a Student's unpaired t-test. In both models, the healthy vessels show minimal k^{trans} divergence (Tofts vs DC-Tofts), 0.0284 ± 0.018 vs 0.0224 ± 0.015, ($p < 0.2337$). Near the aneurysm wall however, DC-Tofts was significantly higher (Tofts vs DC-Tofts), 0.127 ± 0.053, 0.183 ± 0.064, ($p < 0.0060$). In each model, the difference between the healthy vessel wall and aneurysm wall was significant ($p << 0.001$).

Figure **6.6** shows representative images from patients with small, medium, and large aneurysms. Images were chosen to demonstrate the broad range of wall permeability values,

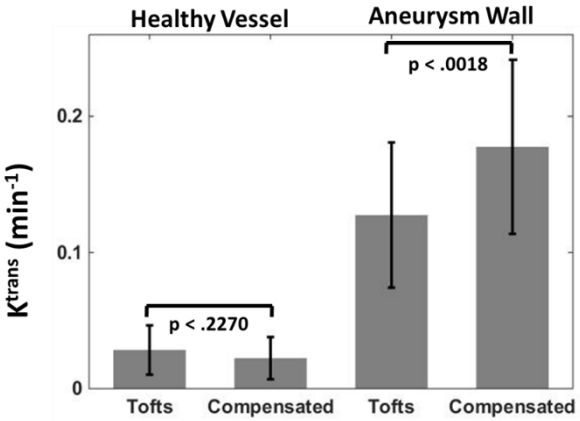

Figure 6.5: Paired t-test shows significance between models. K^{trans}_{DC} shows a statistically significant increase near the aneurysm wall, while k^{trans}_{DC} near healthy vessels is slightly reduced though not significant.

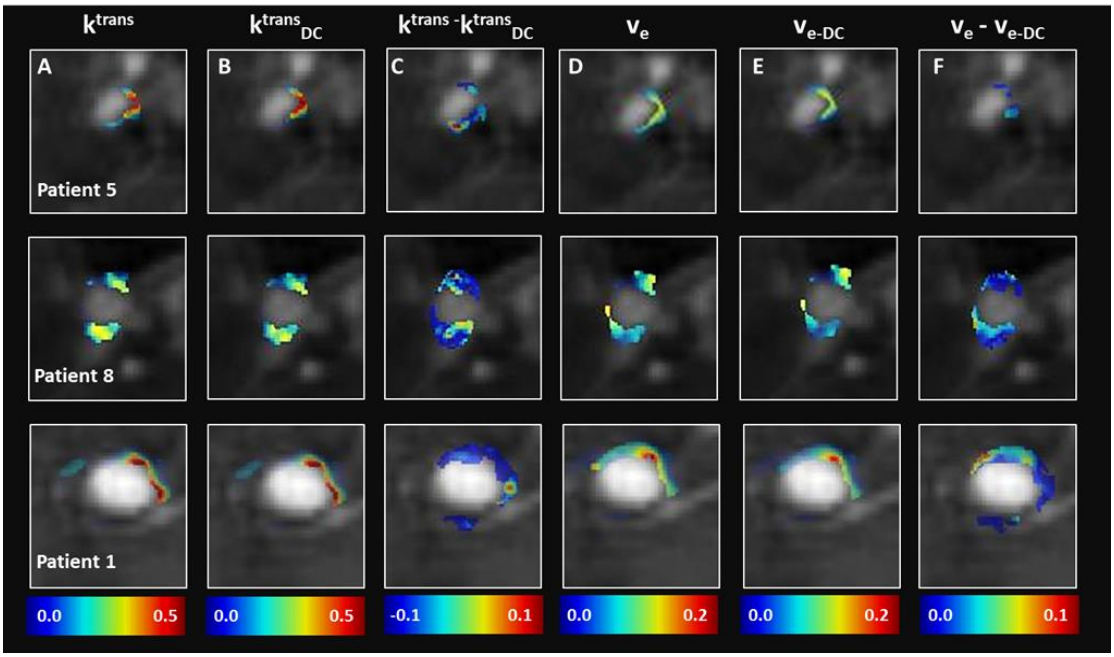

Figure 6.6: Permeability images demonstrate a broad distribution of kinetic values. Representative images chosen from patients with small, medium, and large aneurysms. (A, B, and C) show k^{trans}, k^{trans}_{DC}, and ($k^{trans} - k^{trans}_{DC}$) respectively. (D, E, and F) show v_e, v_{eDC}, and ($v_e - v_{eDC}$).

both among subjects and within a single IA. Figure **6.6**a, b, c, d, e, and f represent k^{trans}, k^{trans}_{DC}, ($k^{trans} - k^{trans}_{DC}$), v_e, v_{eDC}, and ($v_e - v_{eDC}$), respectively.

DC Model Analysis and Parameterization

Diffusion constant, *D*, used in the DC-Tofts model affects k^{trans}_{DC} values near the aneurysm wall, with $k^{trans}_{DC} = k^{trans} + 0.0511\ \sqrt{D}$ (95% CI 0.0453 – 0.0568), Figure **6.7**a. Consequently, previous studies may have under estimated absolute k^{trans}, when a contrast point source is present (i.e. aneurysm wall, leaky tumor vs. necrotic core, etc.). While *D* affected measured k^{trans}_{DC}, it did not affect univariate significance in determining risk (Group A: p = 0.2561 – 0.7139, Group B: p = 0.0232 – 0.0422, Group AB: p = 0.0170 – 0.0295). Figure **6.7**b shows v_{eDC} near the aneurysm wall varies linearly with *D*, $v_{eDC} = v_e - 0.0107*D$ (95% CI 0.0088 – 0.0127).

Figure **6.8** shows the results of the LOOCV analysis. Figure **6.8**a, shows $k^{trans}_{DC} - k^{trans}$ as a function of v_p and *D*. The dots shown are binned means and the surface shown is the fit generated by Equation 42 where (a = 0.2511, b = 0.333, c = 0.01428 and d = 0.02364). As seen before the two models tend to diverge near the aneurysm wall (high v_p) and as *D* increases k^{trans}_{DC} tends to be higher near the wall but lower in the surrounding tissue. Figures **6.8**b through **6.8**e show correlation and Bland Altman alaysis between $k^{trans}_{Corrected}$ and k^{trans}_{DC} both in the surrounding tissue and near the aneurysm wall. $k^{trans}_{Corrected}$ shows very high correlation with k^{trans}_{DC} (surrounding tissue: $r^2 = 0.911$, slope = 0.96149, intercept = 0.01445; wall: $r^2 = 0.899$, slope = 1.0573, intercept = 0.0031).

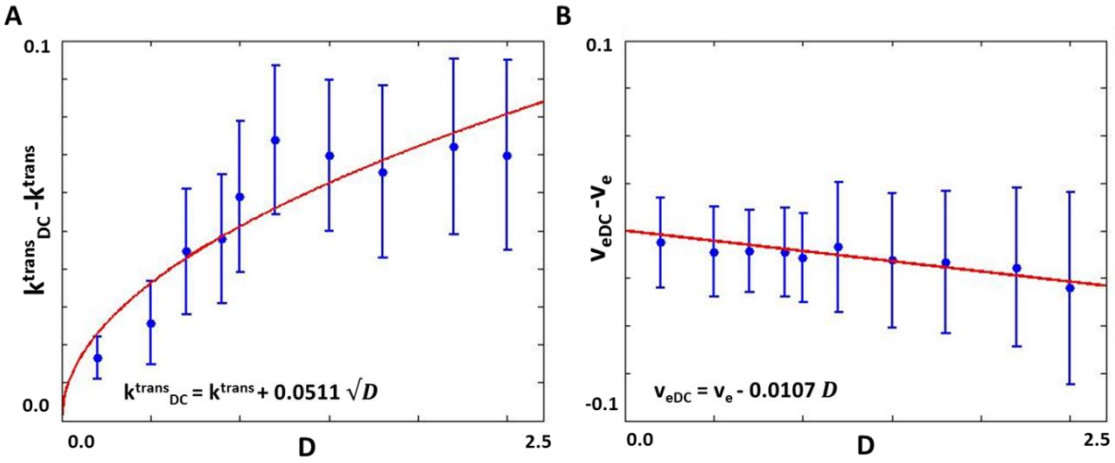

Figure 6.7: Permeability parameters vary with post-processing constant D. k^{trans}_{DC} near the aneurysm wall grows with *D* with $k^{trans}_{DC} = k^{trans} + 0.0511*\sqrt{D}$. (B) Shows v_{eDC} varies linearly near the aneurysm wall, $v_{eDC} = v_e - 0.0107*D$.

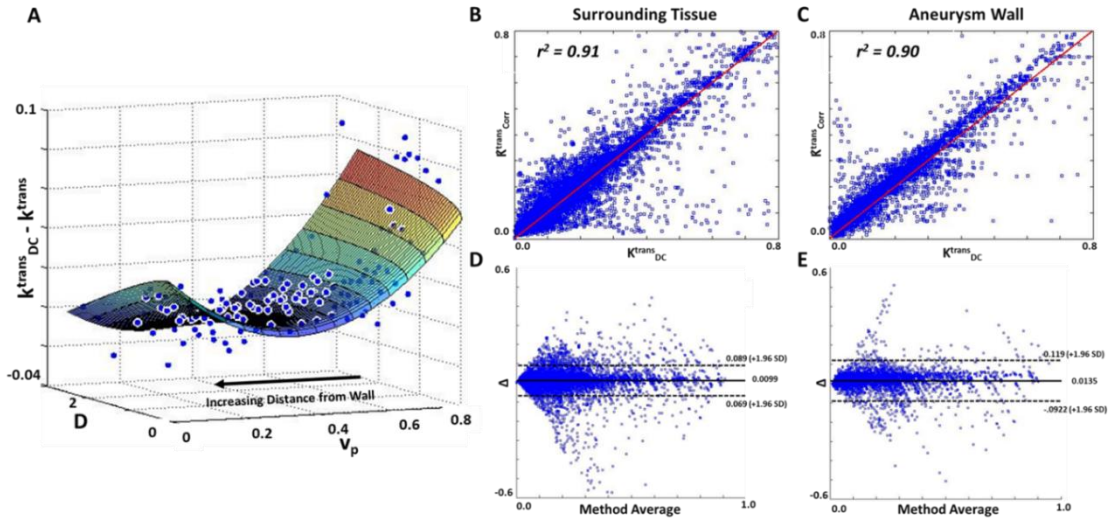

Figure 6.8: LOOCV shows the DC model parameterization improves k^{trans} correlation. (A) Shows $k^{trans}_{DC} - k^{trans}$ as a function of v_p and *D*. Dots shown are binned means and the surface shown is the fit generated by Equation 5. (B and C) Show high correlation between $k^{trans}_{Corrected}$ and k^{trans}_{DC} both in the surrounding tissue and near the aneurysm wall. (D and E) Bland Altman analysis comparing $k^{trans}_{Corrected}$ and k^{trans}_{DC} in surrounding tissue and at the wall.

Patient Demographics

In total 26 aneurysms in 22 patients (<age> = 58.4 ± 11.3 years, age range 30-82 years), 13 women (<age> = 58.8 ± 12.9 years, range 30-76) and 9 men (<age> = 59.3 ± 8.9, range 39-82) were included in the study. There was no significant difference between men and women in age (p<0.92) or IA size (p<0.20). All IAs were unruptured at time of imaging.

Association with Rupture Risk

Table 6 shows the results of univariate and multivariate logistic regression comparing patient age, sex, aneurysm size as well as k^{trans} and ($k^{trans} - k^{trans}_{DC}$) in their ability to predict pre-determined and size-independent high risk saccular IAs in Group A, B, and AB (A or B). Size, k^{trans}, and ($k^{trans} - k^{trans}_{DC}$) showed significant univariate relationships (p<0.05). While k^{trans} was closer to significance in Group A, ($k^{trans} - k^{trans}_{DC}$) was more significant in Group B and Group AB.

Table 6: Results of univariate and multivariate risk analysis.

	Group A (high risk = 6, low risk = 17)			Group B (high risk = 14, low risk = 9)			Group AB (high risk = 16, low risk = 7)		
Univariate Analysis									
Parameter	p-value	coefficient	std error	p-value	coefficient	std error	p-value	coefficient	std error
Sex	0.2132	-1.4917	1.1984	0.6486	0.4055	0.8898	0.8088	-0.2231	0.9220
Age	0.2226	-0.0533	0.0437	0.221	0.0507	0.0415	0.8393	-0.0084	0.0416
IA Size	**0.0317**	**0.2739**	**0.1275**	0.6257	-0.0374	0.0767	0.5614	0.0538	0.0927
K^{trans}	0.0531	17.4574	9.0259	**0.0303**	**23.0784**	**10.6546**	**0.0304**	**36.3299**	**16.7791**
K^{trans}-K^{trans}_{DC}	0.7139	-1.1696	3.1897	**0.0237**	**-19.5151**	**8.5979**	**0.0171**	**-27.2100**	**11.6847**
Multivariate Analysis									
	p-value	coefficient	std error	p-value	coefficient	std error	p-value	coefficient	std error
IA Size	**0.0406**	**0.2395**	**0.1169**	0.1466	-0.1629	0.1122	0.4429	-0.0817	0.1064
K^{trans}	0.1417	18.1565	12.3555	**0.0302**	**32.5074**	**14.9936**	**0.0367**	**42.8838**	**20.5280**
IA Size	**0.0258**	**0.2871**	**0.1288**	0.8161	0.0221	0.0950	0.0867	0.3573	0.2086
K^{trans}-K^{trans}_{DC}	0.3961	-2.8846	3.3989	**0.0252**	**-20.0533**	**8.9583**	**0.0147**	**-46.7818**	**19.1829**
K^{trans}	**0.0499**	**18.8892**	**9.6332**	0.0671	24.2707	13.2557	**0.0053**	**83.1078**	**29.8091**
K^{trans}-K^{trans}_{DC}	0.6547	1.6235	3.6297	**0.0319**	**-21.3202**	**9.9363**	**0.0022**	**-57.9266**	**18.8849**
IA Size	**0.0428**	**0.2426**	**0.1197**	0.648	-0.0478	0.1046	0.1523	0.2858	0.1997
K^{trans}	0.1739	17.6657	12.9905	0.0681	26.002	14.2534	**0.0110**	**56.0028**	**22.0384**
K^{trans}-K^{trans}_{DC}	0.8971	-0.5023	3.8828	0.0655	-19.4838	10.5783	**0.0016**	**-66.5703**	**21.0455**

6.5 Discussion

We found that in DCE-MR permeability examination of IAs, the inclusion of a diffusion term in the Toft's model significantly changes the calculation of contrast kinetics when compare to standard Tofts modelling. Through simulation we presented evidence of contrast agent leakage through the IA wall. Finally, we have shown that a simple estimation of diffusion effects based on readily available ADC tissue values provide a computationally efficient estimate of diffusional transport in MRI (i.e. of k^{trans}_{DC} as a function of tissue specific D, k^{trans} and v_p).

Globally, the both Tofts and DC-Tofts models generate highly correlated k^{trans} and v_e values. However, we see that near the aneurysm wall, the two models diverge. In Figure **6.4**, we noted the greatest difference between the methods as the diffusion compensated model tended to

generate higher values for k^{trans}_{DC} near the aneurysm, while away from the wall k^{trans}_{DC} tended to be slightly lower than Toft's model estimates. This phenomenon is a direct consequence of contrast diffusing away from a boundary source, the aneurysm wall, into the extra cellular matrix.

The original Tofts model does not address contrast-extravasation through the aneurysm wall, which may better represent a macroscopic manifestation of microscopic capillary permeability. In particular, kinetic parameters provided by the Tofts model may reflect both contrast uptake into an inflamed aneurysm wall and the passive diffusion of contrast through a pathologically thinned wall into the CSF. Without the spatial resolution required to directly image the IA wall typically measuring 20-100 microns, an alternative approach to modeling the signal changes associated with pharmacokinetics of the aneurysm wall is required. Previous work hypothesized that thinner IA walls showed higher DCE-MRI wall permeability (i.e. k^{trans} and v_e) (63). In that study, however, k^{trans} and v_e, were derived from the standard Tofts model, preventing the authors from addressing whether contrast was taken up within the wall or if the contrast was leaking through the wall and in turn diffusing away. We examined uptake versus diffusion in Figure **6.3**. Visually, it is very clear that data simulated with negligible diffusion does not match our patient data. Conversely, however, there is clearly a strong association between measured and diffusion (D_{true} = 2.0 x 10^{-3} mm^2/s) data. These results imply that in addition to contrast uptake within the wall, some portion of the contrast must also diffuse through the compromised vasculature and vessel wall.

The univariate and multivariate regression models, show ($k^{trans} - k^{trans}_{DC}$) to be an independent indicator of rupture risk, as defined by imaging/anatomic metrics (Group B and

AB). Interestingly, ($k^{trans} - k^{trans}_{DC}$) did not show significance in distinguishing risk groups in symptomatic patients (Group A). This may be because symptomatic patients are more likely to have active inflammation in the aneurysm wall due to wall remodeling. Active inflammation will result in more contrast uptake within the wall, and possibly less leakage through the wall, which may explain why symptomatic presentations correlated more highly with k^{trans} than with ($k^{trans} - k^{trans}_{DC}$).

Our results taken in concert suggests that the difference between the standard and DC models may quantifying contrast leakage through the wall, implying that ($k^{trans} - k^{trans}_{DC}$) may be a more accurate measure of wall thickness than k^{trans} alone. Consequently, any future study investigating IA remodeling and wall thickness should include both k^{trans} and k^{trans}_{DC} as potential markers.

Limitations

Several limitations were identified in this study. First, in order to reduce computation we estimated a homogenous diffusion constant *D*. Though we analyzed the effects of different *D* estimates, we did not investigate a spatially varying diffusion constant (more representative of tissue heterogeneity). Future work is still required, however, the proposed parameterization of the diffusional effect may allow for the use of ADC values to represent tissue heterogeneity. Secondly, we were limited in our patient data acquisition with a relatively small sample size as well as having data collected from a single institution. Finally, unlike true tissue perfusion and luminal arterial measurements, no readily available reference standard existed for k^{trans} that were within the scope for this work.

6.6 Conclusion

In this pilot study, we present the first evidence of diffusion compensated DCE-MRI modeling of contrast permeability in IAs and propose a parameterization of diffusional effects on kt^{rans}. A comparison of measured against simulated data suggests contrast leakage occurs across the pathologically compromised aneurysm wall into the CSF. Finally, we show that the diffusion compensated wall permeability ($k^{trans} - k^{trans}_{DC}$) may provide an additional bioimaging marker to characterize the rupture risk of IAs in addition to k^{trans} modeling of contrast permeability and uptake into an inflamed aneurysm wall.

Chapter 7 Conclusions

7.1 Conclusions

In this dissertation, we presented an MR-based OEF and CVR technique that requires no contrast. We have showed that MR-PARSE has detectable sensitivity to frequency shifts induced by transient alterations in de-oxyhemoglobin through the cardiac cycle in ICAD patients with greater than 50% stenosis. Furthermore, we demonstrated that through the use of ICA, transient OEF and β are significant predictors of hemispheric compromise. Our approach to quantify transient BOLD fluctuations due to cerebrovascular reactivity represents a new and simple, non-contrast approach to stratifying patients toward therapies to prevent stroke.

We presented evidence of a method to accurately quantitate CVR using current MRI-protocols. We showed that the use of a WCF specific to the second injection allows for accurate quantification of CBF, validated this in a canine model and showed that qCVR can clearly distinguish between stages of hemodynamic compromise.

Finally, we presented evidence of diffusion compensated DCE-MRI modeling of contrast permeability in IAs and proposed a parameterization of diffusional effects on k^{trans}. A comparison of measured versus simulated data suggested contrast leakage occurs across the pathologically compromised aneurysm wall into the CSF. Additionally, we showed that the diffusion compensated wall permeability ($k^{trans} - k^{trans}_{DC}$) may provide a supplementary bioimaging marker to characterize the rupture risk of IAs in addition to k^{trans} modeling of contrast permeability and uptake into an inflamed aneurysm wall.

7.2 Future Work

This body of work shows clear progress toward quantifying stroke risk, however, much work remains. For example, the transient susceptibility MR-OEF technique provides a novel tool for stroke imaging, however, there continues to be multiple avenues for improvement. First, image quality remains poor. In order to image temporally through the cardiac cycle, a fast acquisition was required. For this work we used a rosette trajectory, because of its acquisition of frequency information in 80 ms. However, the image reconstruction remains lacking and consequently, the image quality is relatively poor. Redesigning the pulse sequence from ground up with image quality and speed in mind is an active area of research. One potential design method would implement the forward-backward-forward (FBF) rosette. Furthermore, only 11 patients were imaged, and consequently more data needs to be acquired to confirm our results. One area that we are working on is canine imaging. Canines provide us with known hemodynamic compromises and reference standard microsphere qCVR data.

In this work we showed evidence of MR-qCVR which shows high correlation with the microsphere gold standard. This is an exciting finding. While relative CVR has been around clinically for some time, no quantitative method is available. Consequently, work is needed to determine the exact benefits of quatification. It has been proposed by Nemoto (16) that CVR linearly relates to hemodynamic failure, consequently, qCVR may become the standard for staging hemodynamic compromise. Such a technique may assist clinicians identify patients at high risk for stroke.

Finally, the use of k^{trans}_{DC} as an additional tool when assessing rupture risk and contrast leakage is another intriguing finding. We hypothesize, the difference between the Tofts model

and the diffusion compensated model, correlates with the amount of contrast leaking through the aneurysm wall. This leakage in turn should correlate with wall thickness and rupture risk. Future work that directly measures aneurysm wall thickness and compares it to k^{trans}_{DC} is needed. However, if we are correct, such a finding could be a game changer. Being able to accurately predict rupture risk can stratify patients into surgical cohorts. Furthermore, imaging wall thickness can inform surgeons to problematic regions.

Chapter 8 References

1. Lloyd-Jones D, Adams R, Carnethon M, De Simone G, Ferguson TB, Flegal K, Ford E, Furie K, Go A, Greenlund K and others. Heart disease and stroke statistics--2009 update: a report from the American Heart Association Statistics Committee and Stroke Statistics Subcommittee. Circulation 2009;119(3):480-6.
2. Likosky DS, Marrin CA, Caplan LR, Baribeau YR, Morton JR, Weintraub RM, Hartman GS, Hernandez F, Jr., Braff SP, Charlesworth DC and others. Determination of etiologic mechanisms of strokes secondary to coronary artery bypass graft surgery. Stroke 2003;34(12):2830-4.
3. Carpenter DA, Grubb RL, Jr., Tempel LW, Powers WJ. Cerebral oxygen metabolism after aneurysmal subarachnoid hemorrhage. J Cereb Blood Flow Metab 1991;11(5):837-44.
4. Derdeyn CP, Videen TO, Yundt KD, Fritsch SM, Carpenter DA, Grubb RL, Powers WJ. Variability of cerebral blood volume and oxygen extraction: stages of cerebral haemodynamic impairment revisited. Brain 2002;125(Pt 3):595-607.
5. Weir B. Unruptured intracranial aneurysms: a review. J Neurosurg 2002;96(1):3-42.
6. Ishibashi T, Murayama Y, Urashima M, Saguchi T, Ebara M, Arakawa H, Irie K, Takao H, Abe T. Unruptured intracranial aneurysms: incidence of rupture and risk factors. Stroke 2009;40(1):313-6.
7. Juvela S. Natural history of unruptured intracranial aneurysms: risks for aneurysm formation, growth, and rupture. Acta Neurochir Suppl 2002;82:27-30.
8. Pera J, Korostynski M, Krzyszkowski T, Czopek J, Slowik A, Dziedzic T, Piechota M, Stachura K, Moskala M, Przewlocki R and others. Gene expression profiles in human ruptured and unruptured intracranial aneurysms: what is the role of inflammation? Stroke 2010;41(2):224-31.
9. Glover GH, Noll DC. Consistent projection reconstruction (CPR) techniques for MRI. Magn Reson Med 1993;29(3):345-51.
10. Glover GH, Pauly JM. Projection reconstruction techniques for reduction of motion effects in MRI. Magn Reson Med 1992;28(2):275-89.
11. Funai AK, Fessler JA, Yeo DT, Olafsson VT, Noll DC. Regularized field map estimation in MRI. IEEE Trans Med Imaging 2008;27(10):1484-94.
12. Grissom W, Yip CY, Zhang Z, Stenger VA, Fessler JA, Noll DC. Spatial domain method for the design of RF pulses in multicoil parallel excitation. Magn Reson Med 2006;56(3):620-9.
13. Noll DC, Fessler JA, Sutton BP. Conjugate phase MRI reconstruction with spatially variant sample density correction. IEEE Trans Med Imaging 2005;24(3):325-36.
14. Sutton BP, Noll DC, Fessler JA. Dynamic field map estimation using a spiral-in/spiral-out acquisition. Magn Reson Med 2004;51(6):1194-204.

15. Derdeyn CP, Yundt KD, Videen TO, Carpenter DA, Grubb RL, Jr., Powers WJ. Increased oxygen extraction fraction is associated with prior ischemic events in patients with carotid occlusion. Stroke 1998;29(4):754-8.
16. Nemoto EM, Yonas H, Chang Y. Stages and thresholds of hemodynamic failure. Stroke 2003;34(1):2-3.
17. Raichle ME, MacLeod AM, Snyder AZ, Powers WJ, Gusnard DA, Shulman GL. A default mode of brain function. Proc Natl Acad Sci U S A 2001;98(2):676-82.
18. Yablonskiy DA, Sukstanskii AL, He X. Blood oxygenation level-dependent (BOLD)-based techniques for the quantification of brain hemodynamic and metabolic properties - theoretical models and experimental approaches. NMR Biomed 2012.
19. Yablonskiy DA, Sukstanskii AL, He X. Blood oxygenation level-dependent (BOLD)-based techniques for the quantification of brain hemodynamic and metabolic properties - theoretical models and experimental approaches. NMR Biomed 2013;26(8):963-86.
20. Hodel J, Rodallec M, Gerber S, Blanc R, Maraval A, Caron S, Tyvaert L, Zuber M, Zins M. [Susceptibility weighted magnetic resonance sequences "SWAN, SWI and VenoBOLD": technical aspects and clinical applications]. J Neuroradiol 2012;39(2):71-86.
21. Baker AB, Katsuki S. Stroke: U.S. and Japan. Summary and conclusions. Geriatrics 1969;24(11):124-32.
22. Wong KS, Huang YN, Gao S, Lam WW, Chan YL, Kay R. Intracranial stenosis in Chinese patients with acute stroke. Neurology 1998;50(3):812-3.
23. Sacco RL, Kargman DE, Zamanillo MC. Race-ethnic differences in stroke risk factors among hospitalized patients with cerebral infarction: the Northern Manhattan Stroke Study. Neurology 1995;45(4):659-63.
24. Chimowitz MI, Lynn MJ, Turan TN, Fiorella D, Lane BF, Janis S, Derdeyn CP, Investigators S. Design of the stenting and aggressive medical management for preventing recurrent stroke in intracranial stenosis trial. J Stroke Cerebrovasc Dis 2011;20(4):357-68.
25. Gupta R, Jovin TG. Endovascular management of acute ischemic stroke: advances in patient and treatment selection. Expert Rev Neurother 2007;7(2):143-53.
26. Ascher E, Marks NA, Schutzer RW, Hingorani AP. Duplex-assisted internal carotid artery balloon angioplasty and stent placement: a novel approach to minimize or eliminate the use of contrast material. J Vasc Surg 2005;41(3):409-15.
27. Lansberg MG, Lee J, Christensen S, Straka M, De Silva DA, Mlynash M, Campbell BC, Bammer R, Olivot JM, Desmond P and others. RAPID automated patient selection for reperfusion therapy: a pooled analysis of the Echoplanar Imaging Thrombolytic Evaluation Trial (EPITHET) and the Diffusion and Perfusion Imaging Evaluation for Understanding Stroke Evolution (DEFUSE) Study. Stroke 2011;42(6):1608-14.
28. Kidwell CS, Jahan R, Gornbein J, Alger JR, Nenov V, Ajani Z, Feng L, Meyer BC, Olson S, Schwamm LH and others. A trial of imaging selection and endovascular treatment for ischemic stroke. N Engl J Med 2013;368(10):914-23.
29. Campbell BC, Mitchell PJ, Kleinig TJ, Dewey HM, Churilov L, Yassi N, Yan B, Dowling RJ, Parsons MW, Oxley TJ and others. Endovascular therapy for ischemic stroke with perfusion-imaging selection. N Engl J Med 2015;372(11):1009-18.

30. Saver JL, Goyal M, Bonafe A, Diener HC, Levy EI, Pereira VM, Albers GW, Cognard C, Cohen DJ, Hacke W and others. Stent-retriever thrombectomy after intravenous t-PA vs. t-PA alone in stroke. N Engl J Med 2015;372(24):2285-95.
31. Moskowitz MA, Grotta JC, Koroshetz WJ, Stroke Progress Review G, National Institute of Neurological D, Stroke. The NINDS Stroke Progress Review Group final analysis and recommendations. Stroke 2013;44(8):2343-50.
32. An H, Lin W. Quantitative measurements of cerebral blood oxygen saturation using magnetic resonance imaging. J Cereb Blood Flow Metab 2000;20(8):1225-36.
33. An H, Lin W. Cerebral oxygen extraction fraction and cerebral venous blood volume measurements using MRI: effects of magnetic field variation. Magn Reson Med 2002;47(5):958-66.
34. An H, Lin W. Impact of intravascular signal on quantitative measures of cerebral oxygen extraction and blood volume under normo- and hypercapnic conditions using an asymmetric spin echo approach. Magn Reson Med 2003;50(4):708-16.
35. He X, Yablonskiy DA. Quantitative BOLD: mapping of human cerebral deoxygenated blood volume and oxygen extraction fraction: default state. Magn Reson Med 2007;57(1):115-26.
36. He X, Zhu M, Yablonskiy DA. Validation of oxygen extraction fraction measurement by qBOLD technique. Magn Reson Med 2008;60(4):882-8.
37. Menon RG, Walsh EG, Twieg DB, Cantrell CG, Vakil P, Jonathan SV, Batjer HH, Carroll TJ. Snapshot MR technique to measure OEF using rapid frequency mapping. J Cereb Blood Flow Metab 2014;34(7):1111-6.
38. Twieg DB. Parsing local signal evolution directly from a single-shot MRI signal: a new approach for fMRI. Magn Reson Med 2003;50(5):1043-52.
39. Twieg DB, Reeves SJ. Basic properties of SS-PARSE parameter estimates. IEEE Trans Med Imaging 2010;29(5):1156-72.
40. Zuo J, Bolding M, Twieg DB. Validation of V-SS-PARSE for single-shot flow measurement. Magn Reson Imaging 2007;25(3):335-40.
41. Zuo J, Walsh EG, Deutsch G, Twieg DB. Rapid mapping of flow velocity using a new PARSE method. Magn Reson Med 2006;55(1):147-52.
42. Yablonskiy DA, Haacke EM. Theory of NMR signal behavior in magnetically inhomogeneous tissues: the static dephasing regime. Magn Reson Med 1994;32(6):749-63.
43. Bell AJ, Sejnowski TJ. An information-maximization approach to blind separation and blind deconvolution. Neural Comput 1995;7(6):1129-59.
44. Biswal BB, Ulmer JL. Blind source separation of multiple signal sources of fMRI data sets using independent component analysis. J Comput Assist Tomogr 1999;23(2):265-71.
45. Carroll TJ, Haughton VM, Rowley HA, Cordes D. Confounding effect of large vessels on MR perfusion images analyzed with independent component analysis. AJNR Am J Neuroradiol 2002;23(6):1007-12.
46. Vagal AS, Leach JL, Fernandez-Ulloa M, Zuccarello M. The acetazolamide challenge: techniques and applications in the evaluation of chronic cerebral ischemia. AJNR Am J Neuroradiol 2009;30(5):876-84.

47. Sakaie KE, Shin W, Curtin KR, McCarthy RM, Cashen TA, Carroll TJ. Method for improving the accuracy of quantitative cerebral perfusion imaging. Journal of Magnetic Resonance Imaging 2005;21(5):512-9.
48. Shin W, Cashen TA, Horowitz SW, Sawlani R, Carroll TJ. Quantitative CBV measurement from static T1 changes in tissue and correction for intravascular water exchange. Magnetic Resonance in Medicine 2006;56(1):138-45.
49. Srour JM, Shin W, Shah S, Sen A, Carroll TJ. SCALE-PWI: A pulse sequence for absolute quantitative cerebral perfusion imaging. J Cereb Blood Flow Metab 2010.
50. Hazlewood CF, Chang DC, Nichols BL, Woessner DE. Nuclear magnetic resonance transverse relaxation times of water protons in skeletal muscle. Biophys J 1974;14(8):583-606.
51. Donahue KM, Weisskoff RM, Chesler DA, Kwong KK, Bogdanov AA, Jr., Mandeville JB, Rosen BR. Improving MR quantification of regional blood volume with intravascular T1 contrast agents: accuracy, precision, and water exchange. Magn Reson Med 1996;36(6):858-67.
52. Heydorn K, Damsgaard E, Horn N. Accumulated experience with prenatal diagnosis of Menkes disease by neutron activation analysis of chorionic villi specimens. Biol Trace Elem Res 1999;71-72:551-61.
53. Ostergaard L, Weisskoff RM, Chesler DA, Gyldensted C, Rosen BR. High resolution measurement of cerebral blood flow using intravascular tracer bolus passages. Part I: Mathematical approach and statistical analysis. Magnetic Resonance in Medicine 1996;36(5):715-25.
54. Ostergaard L, Sorensen AG, Kwong KK, Weisskoff RM, Gyldensted C, Rosen BR. High resolution measurement of cerebral blood flow using intravascular tracer bolus passages. Part II: Experimental comparison and preliminary results. Magnetic Resonance in Medicine 1996;36(5):726-36.
55. Vakil P, Lee JJ, Mouannes-Srour JJ, Derdeyn CP, Carroll TJ. Cerebrovascular occlusive disease: quantitative cerebral blood flow using dynamic susceptibility contrast mr imaging correlates with quantitative H2[15O] PET. Radiology 2013;266(3):879-86.
56. Serrador JM, Hughson RL, Kowalchuk JM, Bondar RL, Gelb AW. Cerebral blood flow during orthostasis: role of arterial CO2. Am J Physiol Regul Integr Comp Physiol 2006;290(4):R1087-93.
57. Grandin CB, Bol A, Smith AM, Michel C, Cosnard G. Absolute CBF and CBV measurements by MRI bolus tracking before and after acetazolamide challenge: repeatabilily and comparison with PET in humans. Neuroimage 2005;26(2):525-35.
58. King A, Serena J, Bornstein NM, Markus HS, Investigators A. Does impaired cerebrovascular reactivity predict stroke risk in asymptomatic carotid stenosis? A prospective substudy of the asymptomatic carotid emboli study. Stroke 2011;42(6):1550-5.
59. Kawano T, Ohmori Y, Kaku Y, Muta D, Uekawa K, Nakagawa T, Amadatsu T, Kasamo D, Shiraishi S, Kitajima M and others. Prolonged Mean Transit Time Detected by Dynamic Susceptibility Contrast Magnetic Resonance Imaging Predicts Cerebrovascular Reserve Impairment in Patients with Moyamoya Disease. Cerebrovasc Dis 2016;42(1-2):131-8.

60. Frosen J, Piippo A, Paetau A, Kangasniemi M, Niemela M, Hernesniemi J, Jaaskelainen J. Remodeling of saccular cerebral artery aneurysm wall is associated with rupture: histological analysis of 24 unruptured and 42 ruptured cases. Stroke 2004;35(10):2287-93.
61. Dumont AS, Lanzino G, Kassell NF. Unruptured aneurysms. J Neurosurg 2002;96(1):52-6; discussion 58-60.
62. Hasan DM, Mahaney KB, Magnotta VA, Kung DK, Lawton MT, Hashimoto T, Winn HR, Saloner D, Martin A, Gahramanov S and others. Macrophage imaging within human cerebral aneurysms wall using ferumoxytol-enhanced MRI: a pilot study. Arterioscler Thromb Vasc Biol 2012;32(4):1032-8.
63. Vakil P, Ansari SA, Cantrell CG, Eddleman CS, Dehkordi FH, Vranic J, Hurley MC, Batjer HH, Bendok BR, Carroll TJ. Quantifying Intracranial Aneurysm Wall Permeability for Risk Assessment Using Dynamic Contrast-Enhanced MRI: A Pilot Study. AJNR Am J Neuroradiol 2015;36(5):953-9.
64. Kadasi LM, Dent WC, Malek AM. Cerebral aneurysm wall thickness analysis using intraoperative microscopy: effect of size and gender on thin translucent regions. J Neurointerv Surg 2013;5(3):201-6.
65. Kecskemeti S, Johnson K, Wu Y, Mistretta C, Turski P, Wieben O. High resolution three-dimensional cine phase contrast MRI of small intracranial aneurysms using a stack of stars k-space trajectory. J Magn Reson Imaging 2012;35(3):518-27.
66. Raschi M, Mut F, Byrne G, Putman CM, Tateshima S, Vinuela F, Tanoue T, Tanishita K, Cebral JR. CFD and PIV Analysis of Hemodynamics in a Growing Intracranial Aneurysm. Int j numer method biomed eng 2012;28(2):214-228.
67. Gounis MJ, van der Bom IM, Wakhloo AK, Zheng S, Chueh JY, Kuhn AL, Bogdanov AA, Jr. MR imaging of myeloperoxidase activity in a model of the inflamed aneurysm wall. AJNR Am J Neuroradiol 2015;36(1):146-52.
68. Shi C, Awad IA, Jafari N, Lin S, Du P, Hage ZA, Shenkar R, Getch CC, Bredel M, Batjer HH and others. Genomics of human intracranial aneurysm wall. Stroke 2009;40(4):1252-61.
69. Tofts PS, Brix G, Buckley DL, Evelhoch JL, Henderson E, Knopp MV, Larsson HB, Lee TY, Mayr NA, Parker GJ and others. Estimating kinetic parameters from dynamic contrast-enhanced T(1)-weighted MRI of a diffusable tracer: standardized quantities and symbols. J Magn Reson Imaging 1999;10(3):223-32.
70. Tofts PS. Optimal detection of blood-brain barrier defects with Gd-DTPA MRI-the influences of delayed imaging and optimised repetition time. Magn Reson Imaging 1996;14(4):373-80.
71. Nielsen T, Wittenborn T, Horsman MR. Dynamic Contrast-Enhanced Magnetic Resonance Imaging (DCE-MRI) in Preclinical Studies of Antivascular Treatments. Pharmaceutics 2012;4(4):563-89.
72. Barrett T, Brechbiel M, Bernardo M, Choyke PL. MRI of tumor angiogenesis. J Magn Reson Imaging 2007;26(2):235-49.
73. Barrett T, Kobayashi H, Brechbiel M, Choyke PL. Macromolecular MRI contrast agents for imaging tumor angiogenesis. Eur J Radiol 2006;60(3):353-66.

74. O'Connor JP, Jackson A, Parker GJ, Jayson GC. DCE-MRI biomarkers in the clinical evaluation of antiangiogenic and vascular disrupting agents. Br J Cancer 2007;96(2):189-95.
75. Padhani AR, Husband JE. Dynamic contrast-enhanced MRI studies in oncology with an emphasis on quantification, validation and human studies. Clin Radiol 2001;56(8):607-20.
76. Larsson HB, Courivaud F, Rostrup E, Hansen AE. Measurement of brain perfusion, blood volume, and blood-brain barrier permeability, using dynamic contrast-enhanced T(1)-weighted MRI at 3 tesla. Magn Reson Med 2009;62(5):1270-81.
77. Singh A, Haris M, Rathore D, Purwar A, Sarma M, Bayu G, Husain N, Rathore RK, Gupta RK. Quantification of physiological and hemodynamic indices using T(1) dynamic contrast-enhanced MRI in intracranial mass lesions. J Magn Reson Imaging 2007;26(4):871-80.
78. Fluckiger JU, Loveless ME, Barnes SL, Lepage M, Yankeelov TE. A diffusion-compensated model for the analysis of DCE-MRI data: theory, simulations and experimental results. Phys Med Biol 2013;58(6):1983-98.
79. Pellerin M, Yankeelov TE, Lepage M. Incorporating contrast agent diffusion into the analysis of DCE-MRI data. Magn Reson Med 2007;58(6):1124-34.
80. Heye AK, Culling RD, Valdes Hernandez Mdel C, Thrippleton MJ, Wardlaw JM. Assessment of blood-brain barrier disruption using dynamic contrast-enhanced MRI. A systematic review. Neuroimage Clin 2014;6:262-74.
81. MacDonald DJ, Finlay HM, Canham PB. Directional wall strength in saccular brain aneurysms from polarized light microscopy. Ann Biomed Eng 2000;28(5):533-42.
82. Scott S, Ferguson GG, Roach MR. Comparison of the elastic properties of human intracranial arteries and aneurysms. Can J Physiol Pharmacol 1972;50(4):328-32.
83. Suzuki J, Ohara H. Clinicopathological study of cerebral aneurysms. Origin, rupture, repair, and growth. J Neurosurg 1978;48(4):505-14.
84. Maki JH, Chenevert TL, Prince MR. Three-dimensional contrast-enhanced MR angiography. Top Magn Reson Imaging 1996;8(6):322-44.
85. Deoni SC. High-resolution T1 mapping of the brain at 3T with driven equilibrium single pulse observation of T1 with high-speed incorporation of RF field inhomogeneities (DESPOT1-HIFI). J Magn Reson Imaging 2007;26(4):1106-11.
86. Fram EK, Herfkens RJ, Johnson GA, Glover GH, Karis JP, Shimakawa A, Perkins TG, Pelc NJ. Rapid calculation of T1 using variable flip angle gradient refocused imaging. Magn Reson Imaging 1987;5(3):201-8.
87. Helenius J, Soinne L, Perkio J, Salonen O, Kangasmaki A, Kaste M, Carano RA, Aronen HJ, Tatlisumak T. Diffusion-weighted MR imaging in normal human brains in various age groups. AJNR Am J Neuroradiol 2002;23(2):194-9.

Chapter 9 Appendices

9.1 Appendix A:

Our derivation of the vascular residue function (VRF) is similar in concept to a 2-element Windkessel model which describes flow, Q(t), and pressure, P(t), in the cardiovascular system as input and output signals to the system, respectively. We begin with flow continuity, which requires

$$\frac{dV(t)}{dt} = Q_{in}(t) - Q_{out}(t)$$

with V equal to blood volume and Q the corresponding flow. Q_{out} is related to pressure by the downstream vascular/capillary resistance,

$$Q_{out}(t) = \frac{P(t)}{R}$$

where P is the pressure drop across the resistance bed. With compliance defined as the change in volume due to a change in pressure (dV/dP), we can solve to get

$$Q(t) = \frac{P(t)}{R} + C\frac{dP(t)}{dt}$$

By estimating Q(t) as an impulse function we can solve P(t) during diastole.

$$P(t) = P_0 e^{-t/RC}$$

Then by taking the derivative of above equation, we can solve for the change in blood volume with time during diastole.

$$\frac{dV(t)}{dt} = \frac{P_0}{R} e^{-t/RC} = VRF$$

In the more realistic setting where Q(t) is not an impulse function, the dynamic BOLD signal we acquire becomes

$$Q(t) * VRF = \Delta\delta\omega(t)$$

Where $\Delta\delta\omega(t)$, the fluctuation from baseline $\delta\omega$, is equal to Q(t) convolved with the tissue specific VRF.